Cohesive Zone Models: A Critical Review of Traction-Separation Relationships Across Fracture Surfaces

Kyoungsoo Park

School of Civil & Environmental Engineering,
Yonsei University,
50 Yonsei-ro, Seodaemun-gu,
Seoul, Korea
e-mail: k-park@yonsei.ac.kr

Glaucio H. Paulino[1]

Department of Civil &
Environmental Engineering,
University of Illinois at Urbana-Champaign,
205 North Mathews Avenue,
Urbana, IL 61801
e-mail: paulino@illinois.edu

One of the fundamental aspects in cohesive zone modeling is the definition of the traction-separation relationship across fracture surfaces, which approximates the nonlinear fracture process. Cohesive traction-separation relationships may be classified as either nonpotential-based models or potential-based models. Potential-based models are of special interest in the present review article. Several potential-based models display limitations, especially for mixed-mode problems, because of the boundary conditions associated with cohesive fracture. In addition, this paper shows that most effective displacement-based models can be formulated under a single framework. These models lead to positive stiffness under certain separation paths, contrary to general cohesive fracture phenomena wherein the increase of separation generally results in the decrease of failure resistance across the fracture surface (i.e., negative stiffness). To this end, the constitutive relationship of mixed-mode cohesive fracture should be selected with great caution. [DOI: 10.1115/1.4023110]

1 Introduction

A fundamental issue in the simulation of cohesive failure mechanisms is the definition of cohesive interactions along fracture surfaces. Cohesive interactions approximate progressive nonlinear fracture behavior, named as the cohesive zone model (see Fig. 1). Cohesive interactions are generally a function of displacement jump (or separation). If the displacement jump is greater than a characteristic length (δ_n), complete failure occurs (i.e., no load-bearing capacity). Notice that the cohesive zone model is not limited to modeling a single crack tip, but is also able to describe crack nucleation and pervasive cracking through various time and length scales.

The cohesive constitutive relationships can be classified as either nonpotential-based models or potential-based models. Nonpotential-based cohesive interaction models are relatively simple to develop, because a symmetric system is not required [1–3]. However, these models do not guarantee consistency of the constitutive relationship for arbitrary mixed-mode conditions, because they do not account for all possible separation paths.

For potential-based models, the traction-separation relationships across fracture surfaces are obtained from a potential function, which characterizes the fracture behavior. Note that the existence of a potential for the cohesive constitutive relationship is addressed in conjunction with the non-negative work for closed processes [1,2]. Due to the nature of a potential, the first derivative of the fracture energy potential (Ψ) provides the traction (cohesive interactions) over fracture surfaces, and its second derivative provides the constitutive relationship (material tangent modulus). Several potential-based models are available in the literature; such as, models with specific polynomial orders [4,5], models with exponential expressions [6–9], and a model with general polynomials [3]. Each model possesses advantages and limitations. The present paper critically reviews traction-separation relationships of cohesive fracture with an emphasis on potential-based constitutive models.

There are generally required characteristics for cohesive constitutive relationships, which are summarized as follows:

- The traction separation relationship is independent of any superposed rigid body motion.
- The work to create a new surface is finite, and its value corresponds to the fracture energy, i.e., area under a traction-separation curve.
- The mode I fracture energy is usually different from the mode II fracture energy.
- A finite characteristic length scale exists, which leads to a complete failure condition, i.e., no load-bearing capacity.
- The cohesive traction across the fracture surface generally decreases to zero while the separation increases under the softening condition, which results in the negative stiffness.
- A potential for the cohesive constitutive relationship may exist, and thus the energy dissipation associated with unloading/reloading is independent of a potential.

The remainder of this paper is organized as follows. In the next section, related works are briefly mentioned. Section 3 presents
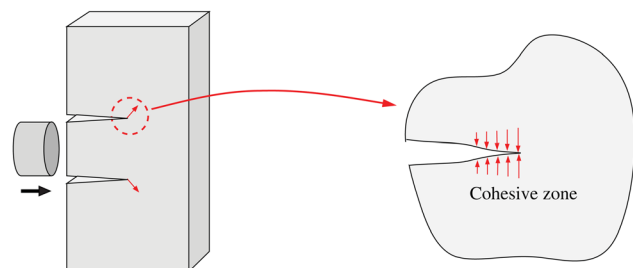

Fig. 1   Schematics of the cohesive zone model

one-dimensional effective displacement-based models and illustrates that the models can be formulated under a single framework. Section 4 provides a context on general potential-based models, which are also discussed in the following sections. Section 5 reviews potential-based models with specific polynomial orders, while Sec. 6 discusses potential-based models with exponential expressions. A unified potential-based model is reviewed in Sec. 7. Finally, essential aspects of potential-based cohesive zone models are summarized in Sec. 8.

2 Related Work

Cohesive zone models have been utilized to mitigate stress singularities in linear elastic fracture mechanics and to approximate nonlinear material separation phenomena [10–14]. In this regard, Elliott [15] conceived nonlinear material failure and introduced an interatomic attracting force per unit area to investigate fracture of a crystalline substance along a cleavage plane. Later, the concept of the cohesive zone model was presented by Barenblatt [16,17] to account for finite strength of brittle materials. Dugdale [18] employed a similar cohesive zone model to investigate yielding at a crack tip and size of the plastic zone. The cohesive traction along the cohesive zone was assumed to be constant when the separation was smaller than a critical value. In these early works, the cohesive zone model was introduced to account for nonlinear fracture behavior, and the model was equivalent to the Griffith's energy balance concept [19] when the size of the cohesive zone was small compared to crack-size and specimen geometry [20,21].

The concept of the cohesive zone model has been widely employed to investigate various material failure phenomena. For elastic-plastic analysis of linear elastic cracked problems under small scale yielding conditions, the plastic zone size has been approximated for various configurations in conjunction with the cohesive zone model [22–25]. In addition, by utilizing the assumption that cohesive tractions exist along crack surfaces, which are smoothly joined together [17], Keer [26] determined the stress distribution within the framework of classical elasticity theory. Based on Keer's approach, Cribb and Tomkins [27] obtained a cohesive force versus separation relationship, which satisfies an assumed stress distribution at the crack tip of a perfectly brittle material. Later, Smith [28] developed a generalized theory and provided a series of traction-separation relationships based on simple expressions for displacements along the crack tip.

In order to consider a relatively large nonlinear fracture process zone in quasi-brittle materials such as concrete, rocks and fiber-reinforced concrete, the cohesive zone model (also called the fictitious crack model) has been employed [29–33]. Hillerborg et al. [29] introduced a linear softening model, which was defined by the fracture energy and the tensile strength of concrete. Later, bilinear softening models [32,34–37] were extensively utilized to investigate concrete fracture and its size effect in conjunction with two fracture energy quantities (i.e., initial fracture energy and total fracture energy) [38–42]. In addition, the fracture process of fiber reinforced concrete has been studied by considering two failure mechanisms: one associated with plain concrete and the other with fibers [43,44].

Crazing of polymers has been represented by using the cohesive zone model [45]. The crazing process may consist of three stages: initiation, widening and breakdown of fibrils [46]. Such microstructural craze response was approximated by a macroscopic crack in conjunction with the concept of the cohesive zone model [47,48]. A representative volume element, extracted from the crazing process zone, was idealized as fibrils that are surrounded by air, and a homogenized cohesive traction-separation relationship was obtained [49]. Additionally, a relation between craze failure and craze microstructural quantities was identified in conjunction with molecular dynamics simulations, which led to a connection between cohesive and molecular parameters [50,51]. The shape of the cohesive traction-separation curve of crazing in glassy polymers was obtained by integrating electronic speckle pattern interferometry and an analytical inverse technique [52].

The cohesive zone model has also been utilized to account for the effect of microstructure on macroscopic response. Heterogeneities of a material were modeled by embedding cohesive interfaces in a random mesh consisting of Voronoi cell elements [53–55]. Additionally, intergranular cracking and matrix/particle debonding within a representative volume element were described by means of the cohesive traction-separation relations [9,56–59]. For example, effects of an interphase region on debonding were investigated for a carbon nanotube reinforced polymer composite [58]. Micromechanics and a finite element-based cohesive zone model were integrated to study the constitutive relationship of materials with microstructures [59].

Failure of functionally graded materials (FGM) has been investigated by several approaches [60]. Based on linear elastic fracture mechanics, mixed boundary-value problems of FGMs have been solved [61–64]. Alternatively, cohesive zone models have been utilized to account for elastic-plastic cracks [65,66] including brittle to ductile transition [67], thermal cracks [68], and dynamic fracture [69,70]. For example, a phenomenological traction-based cohesive zone model was proposed in conjunction with a volume fraction approach for metal-ceramic FGMs [67,71]. A tailored volume-fraction-based cohesive zone model, with some experimental validation, was also developed for investigating fracture of functionally graded fiber-reinforced concrete materials [44]. The traction-based model was extended to a displacement-based cohesive zone model in order to investigate J resistance behavior [72], establishing a connection between cohesive zone and J-integral for FGMs.

Furthermore, the cohesive zone model has been utilized to investigate failure phenomena [73] associated with various time and length scales, such as fatigue crack growth [74–78], bond-slip in reinforced concrete [79–81], crack growth along adhesive bond joints [82–85], microbranching instability [86–88], fragmentation phenomena [89–91], etc.

During the progressive cohesive failure process, the amount of dissipated energy per unit area generally depends on the mode-mixity [12]. The variation of the fracture energy from mode I and mode II was demonstrated by employing mixed-mode fracture tests [92–95]. For example, Zhu et al. [95] obtained traction-separation relationships for mode I and mode II fracture of adhesives, and illustrated that the mode II fracture energy is approximately two times greater than the mode I fracture energy. Additionally, the concept of an anisotropic failure surface was presented in order to account for mixed-mode failure in elastic materials [45]. Thus, it is essential for the traction-separation relationship to capture different fracture energies with respect to the mode-mixity.

Such cohesive failure investigations have been generally performed in conjunction with computational techniques to approximate the nonlinear fracture process. For example, Hillerborg et al. [29] combined the cohesive zone model with the finite element method (FEM) for the analysis of quasi-brittle materials (e.g., concrete) through an equivalent nodal force corresponding to a linear traction-separation relationship. Alternatively, cohesive surface elements were introduced to describe material separation and the traction-separation relationship [96,97]. One may embed cohesive surface elements within the potential failure domain before computational simulation, so-called the intrinsic cohesive zone model [67,69,96]. On the other hand, cohesive surface elements can be adaptively inserted during computational simulation whenever and wherever they are needed [87,97,98]. This approach is known as the extrinsic cohesive zone model. Note that in order to efficiently and effectively handle adaptive mesh modification, a robust topology-based data structure is needed [99–102]. Instead of utilizing surface elements, in generalized/extended finite element methods (GFEM/XFEM) [103–105], a crack geometry can be represented by discontinuous shape functions. Notice that the representation of a three-dimensional arbitrary crack geometry
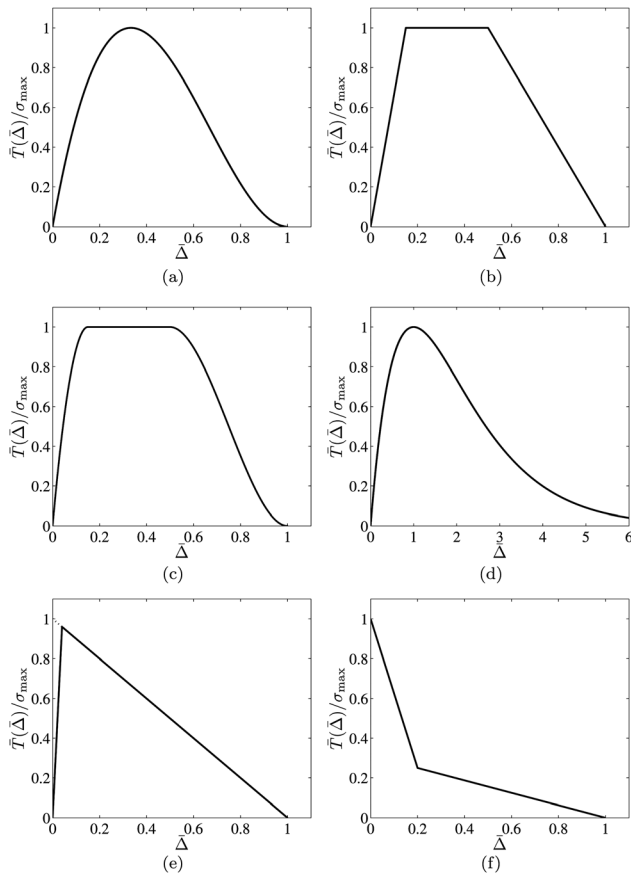
Fig. 2 Effective traction-separation relationships: (a) cubic polynomial, (b) trapezoidal, (c) smoothed trapezoidal, (d) exponential, (e) linear softening, and (f) bilinear softening

with discontinuous shape functions is still a challenging research area [55,106,107]. There are also other available computational frameworks such as finite element with embedded strong discontinuity [108–110], plasticity-based interface fracture models [111–114], virtual internal bond methods [115–117], microplane models [118–120], peridynamics [121–123], etc. Notice that the choice of computational techniques is usually independent of the choice of the constitutive relationship of cohesive fracture. However, if one employs the intrinsic cohesive zone model, an initial elastic range is required for the constitutive relationship.

Cohesive traction-separation relationships may be obtained by employing theoretical, experimental and computational techniques. For example, based on the J-integral approach, a traction-separation relation was obtained for double cantilever beam specimens [124]. Inverse analyses were employed to calibrate a traction-separation relationship so that the best predicted global load-displacement curve was achieved [125–127]. Based on a measured local displacement field, digital image correlation techniques and inverse analysis were employed to estimate fracture parameters and determine traction-separation relationships [52,128–130]. Additionally, macroscopic traction-separation relationships were also obtained by considering microstructure in

conjunction with multiscale analysis [131–134]. The present review paper focuses on cohesive traction-separation relationships, which are expressed in closed form and are able to describe general mixed-mode failure.

3 One-Dimensional Effective Displacement-Based Models

Several constitutive relationships of the cohesive zone model have been developed on the basis of an effective displacement ($\bar{\Delta}$) and an effective traction ($\bar{T}$). The effective displacement and traction easily define various cohesive relations such as cubic polynomial [135], trapezoidal [136], smoothed trapezoidal [137], exponential [98], linear softening [97,138,139] and bilinear softening [34,35] functions, as shown in Fig. 2. Note that the effective traction is normalized with the cohesive strength (σ_{max}) in Fig. 2. Such one-dimensional effective displacement-traction relationships are employed to investigate mixed-mode fracture problems, and can be formulated within a single framework, which is essentially based on the interpretation of a scaling parameter (called α_e below). Table 1 summarizes the models discussed within this framework.

Tvergaard [135] introduced an effective displacement-based model by relating the effective quantities ($\bar{T}, \bar{\Delta}$) to the normal and tangential tractions, as follows:

$$T_n = \frac{\bar{T}(\bar{\Delta})}{\bar{\Delta}} \frac{\Delta_n}{\delta_n}, \quad T_t = \frac{\bar{T}(\bar{\Delta})}{\bar{\Delta}} \alpha_e \frac{\Delta_t}{\delta_t} \qquad (1)$$

where α_e is a nondimensional constant associated with mode-mixity, and δ_n and δ_t are normal and tangential characteristic lengths associated with the fracture energy and the cohesive strength. A nondimensional effective displacement ($\bar{\Delta}$) is defined as

$$\bar{\Delta} = \sqrt{(\Delta_n/\delta_n)^2 + (\Delta_t/\delta_t)^2} \qquad (2)$$

where Δ_n and Δ_t are normal and tangential separation variables, respectively. An effective traction $\bar{T}(\bar{\Delta})$ defines the shape of the traction-separation relation. Tvergaard [135] employed a cubic polynomial function (Fig. 2(a)) for the effective traction ($\bar{T}$), i.e.,

$$\bar{T}(\bar{\Delta}) = \frac{27}{4} \sigma_{max} \bar{\Delta}(1 - 2\bar{\Delta} + \bar{\Delta}^2) \qquad (3)$$

that corresponds to the normal cohesive traction proposed by Needleman [4], which is discussed later in this paper (see Sec. 5.1). In addition, the normal cohesive traction (T_n) is the same as $\bar{T}(\bar{\Delta})$ for the mode I case ($\Delta_t = 0$), while the tangential cohesive traction (T_t) is identical to $\alpha_e \bar{T}(\bar{\Delta})$ for the mode II case ($\Delta_n = 0$), see Eq. (1). Thus, the nondimensional constant (α_e) is a scaling factor between tangential and normal cohesive tractions.

3.1 Model by Tvergaard and Hutchinson and its Extensions. Equation (1) is able to represent other traction-separation relationships by modifying the effective traction ($\bar{T}$) and the nondimensional constant (α_e). For example, the one-dimensional traction potential-based model by Tvergaard and Hutchinson [136] is expressed as

Table 1 Framework for one-dimensional effective models based on Eq. (1)

Models	α_e	Traction-separation relationship
Tvergaard [135]	arbitrary (e.g., $\alpha_e = 1$)	Cubic polynomial
Tvergaard and Hutchinson [136]	δ_n/δ_t	Trapezoidal
Ortiz and Pandolfi [98]	δ_n/δ_t	Linear without the initial slope
Geubelle and Baylor [138]	τ_{max}/σ_{max}	Linear with the initial slope

$$\Psi = \delta_n \int_0^{\bar{\Delta}} \bar{T}(\bar{\delta}) d\bar{\delta} \tag{4}$$

The derivative of the potential (Eq. (4)) leads to the cohesive traction vector,

$$T_n = \frac{\partial \Psi}{\partial \bar{\Delta}} \frac{\partial \bar{\Delta}}{\partial \Delta_n} = \frac{\bar{T}(\bar{\Delta})}{\bar{\Delta}} \frac{\Delta_n}{\delta_n}, \quad T_t = \frac{\partial \Psi}{\partial \bar{\Delta}} \frac{\partial \bar{\Delta}}{\partial \Delta_t} = \frac{\bar{T}(\bar{\Delta})}{\bar{\Delta}} \frac{\delta_n}{\delta_t} \frac{\Delta_t}{\delta_t} \tag{5}$$

which is a special case of Eq. (1) when the nondimensional constant is given by

$$\alpha_e = \frac{\delta_n}{\delta_t} \tag{6}$$

Note that the one-dimensional traction potential leads to the symmetric system, i.e., exact differential

$$\frac{\partial T_n}{\partial \Delta_t} = \frac{\partial T_t}{\partial \Delta_n} \tag{7}$$

however, the model is unable to account for different fracture energies along the normal and tangential directions [136].

Based on the one-dimensional traction potential-based model (Eq. (4)), trapezoidal shape models (Fig. 2(b)) have been used for elasto-plastic materials [136,140–142]. In order to provide continuity in the derivative of the traction-separation relationship, the trapezoidal shape is modified [137], as shown in Fig. 2(c). Alternatively, the universal binding energy by Rose et al. [143] was also employed for the one-dimensional traction potential-based model (see Fig. 2(d)), which is given as

$$\Psi = \delta_n \int_0^{\bar{\Delta}} e\sigma_{\max} \bar{\delta} e^{\bar{\delta}} d\bar{\delta} = e\sigma_{\max} \delta_n \left[1 - \left(1 + \bar{\Delta}\right) e^{-\bar{\Delta}} \right] \tag{8}$$

The model has been used to investigate crack propagation of C-300 steel [98], functionally graded materials [67,69], and asphalt concrete [144].

3.2 Model by Ortiz and Pandolfi. Based on a free energy density per unit area, Ortiz and Pandolfi [98] defined the cohesive traction vector (**T**),

$$\mathbf{T} = \frac{\widetilde{T}(\widetilde{\Delta})}{\widetilde{\Delta}} \left(\beta_e^2 \mathbf{\Delta}_t + \Delta_n \mathbf{n}_n \right) \tag{9}$$

where $\mathbf{n}_n$ is a unit normal vector to a cohesive surface, and $\mathbf{\Delta}_t$ is an in-plane tangential separation vector. The above cohesive traction vector may be decomposed as

$$T_n = \frac{\widetilde{T}(\widetilde{\Delta})}{\widetilde{\Delta}} \Delta_n, \quad T_t = \frac{\widetilde{T}(\widetilde{\Delta})}{\widetilde{\Delta}} \Delta_t \beta_e^2 \tag{10}$$

Note that the in-plane tangential separation vector ($\mathbf{\Delta}_t$) is equal to $\Delta_t \mathbf{n}_t$ where $\mathbf{n}_t$ is a unit in-plane tangential separation vector. In addition, the effective displacement is defined as $\widetilde{\Delta} = \sqrt{\Delta_n^2 + \beta_e^2 \Delta_t^2}$, which is dimensional (rather than nondimensional) [97,98], where β_e is a nondimensional constant associated with mode-mixity. Both $\bar{\Delta}$ and $\widetilde{\Delta}$ are equivalent, i.e.,

$$\bar{\Delta} = \widetilde{\Delta}/\delta_n \quad \text{when} \quad \beta_e = \delta_n/\delta_t \tag{11}$$

which, again, corresponds to the general format of Eq. (1) when $\alpha_e = \beta_e$. For the effective traction separation relationship, $\widetilde{T}(\widetilde{\Delta})$, Camacho and Ortiz [97] employed a linear softening model, which does not include the initial elastic range in the constitutive

relationship, leading to the so-called extrinsic cohesive zone model. Ortiz and Pandolfi [98] indicated that in explicit calculations, a cohesive law of the linear softening model without the initial elastic range is preferable to one of the exponential model (i.e., Eq. (8)), as the initial elastic slope in the latter may place stringent restrictions on the stable time step for explicit integrations. The model was utilized to study dynamic fragmentation [90] and microbranching instability [87].

3.3 Model by Geubelle and Baylor. The linear softening model (Fig. 2(e)) by Geubelle and Baylor [138] is a special case of Eq. (1). The normal and tangential tractions of the bilinear cohesive traction model are originally given as

$$T_n = \sigma_{\max} \frac{D_s}{1 - D_s} \frac{\Delta_n}{\delta_n}, \quad T_t = \tau_{\max} \frac{D_s}{1 - D_s} \frac{\Delta_t}{\delta_t} \tag{12}$$

where $\sigma_{\max}$ is the normal cohesive strength, and $\tau_{\max}$ is the tangential cohesive strength. An internal residual strength variable (D_s) is defined as $D_s = \min(D_{\min}, \max(0, 1 - \bar{\Delta}))$, which controls complete failure and unloading/reloading conditions. An internal variable ($D_{\min}$) is related to the value of the effective displacement when the cohesive traction reaches the cohesive strength. If $\bar{\Delta}$ is smaller than $(1 - D_{\min})$, the cohesive traction linearly increases with respect to the increase of separation, which corresponds to the artificial initial elastic range in the intrinsic model. For the softening condition ($\bar{\Delta} > 1 - D_{\min}$), the cohesive traction is expressed as

$$T_n = \sigma_{\max} \frac{1 - \bar{\Delta}}{\bar{\Delta}} \frac{\Delta_n}{\delta_n}, \quad T_t = \tau_{\max} \frac{1 - \bar{\Delta}}{\bar{\Delta}} \frac{\Delta_t}{\delta_t} \tag{13}$$

which corresponds to Eq. (1) when

$$\bar{T} = \sigma_{\max}(1 - \bar{\Delta}), \quad \alpha_e = \tau_{\max}/\sigma_{\max} \tag{14}$$

The model has been utilized for failure of polycrystalline brittle materials [139] and viscoelastic asphalt concrete [145,146].

3.4 Extension to Three-Dimensional Problems. The one-dimensional effective displacement model of Eq. (1) has also been extended to investigate three-dimensional cohesive zone models [98,147]. In this case, the effective displacement is defined as

$$\bar{\Delta} = \sqrt{\left(\Delta_1/\delta_1\right)^2 + \left(\Delta_2/\delta_2\right)^2 + \left(\Delta_3/\delta_3\right)^2} \tag{15}$$

where Δ_1, Δ_2, and Δ_3 are separations, and δ_1, δ_2, and δ_3 are characteristic lengths along the local coordinates, as shown in Fig. 3.
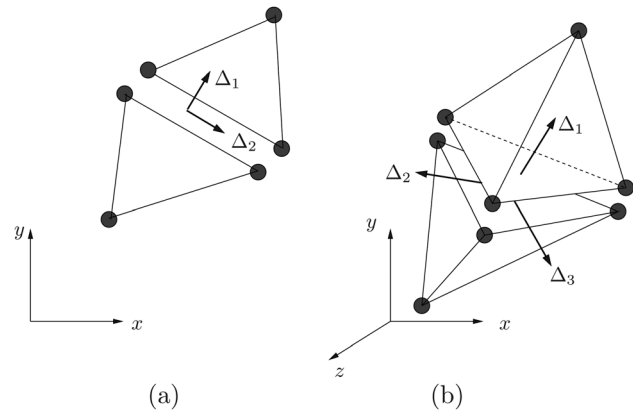

Fig. 3 Cohesive fracture separations along the local coordinate system (a) two-dimensions (Δ_1, Δ_2) and (b) three-dimensions (Δ_1, Δ_2, Δ_3)

Note that the subscript 1 denotes opening mode, while the subscripts 2 and 3 indicate two in-plane shear modes. Accordingly, the cohesive traction vector is defined as

$$T_1 = \frac{\bar{T}(\bar{\Delta})}{\bar{\Delta}}\frac{\Delta_1}{\delta_1}, \quad T_2 = \frac{\bar{T}(\bar{\Delta})}{\bar{\Delta}}\alpha_2\frac{\Delta_2}{\delta_2}, \quad T_3 = \frac{\bar{T}(\bar{\Delta})}{\bar{\Delta}}\alpha_3\frac{\Delta_3}{\delta_3} \quad (16)$$

where α_2 and α_3 are nondimensional constants associated with mode-mixity.

3.5 Limitations of Effective Displacement-Based Models.
The previously discussed effective displacement-based models possess certain limitations. Namely, they can provide positive stiffness under softening condition. In other words, the cohesive traction increases while the separation increases, which is generally an undesirable traction-separation relationship (unless the material demonstrates stiffening behavior while separation increases). This fact is demonstrated as follows. The derivative of the normal traction (Eq. (1)) with respect to the normal separation (Δ_n) leads to

$$\frac{\partial T_n}{\partial \Delta_n} = \frac{1}{\delta_n \bar{\Delta}}\left\{\bar{T} + \left(\frac{\Delta_n}{\delta_n \bar{\Delta}}\right)^2\left(\frac{\partial \bar{T}}{\partial \bar{\Delta}}\bar{\Delta} - \bar{T}\right)\right\} \quad (17)$$

Let us assume the effective traction ($\bar{T}$) as a linearly decreasing line, i.e., $\bar{T} = \sigma_{max}(1 - \bar{\Delta})$. The substitution of the linear effective traction into Eq. (17) results in

$$\frac{\partial T_n}{\partial \Delta_n} = \frac{\sigma_{max}}{\delta_n}\frac{1}{\bar{\Delta}}\left\{1 - \bar{\Delta} - \left(\frac{\Delta_n}{\delta_n \bar{\Delta}}\right)^2\right\} \quad (18)$$

When Δ_t is zero (i.e., mode I), the stiffness of the normal cohesive traction is $-\sigma_{max}/\delta_n$, as expected. However, when Δ_n is zero (i.e., mode II), the stiffness of the normal cohesive traction is $(\delta_t/\Delta_t - 1)\sigma_{max}/\delta_n$, which is greater than zero. Therefore, the normal cohesive traction can increase while the normal or tangential separation increases. The normal cohesive traction and its stiffness (Eq. (18)) are plotted in Fig. 4. One can clearly observe the positive stiffness in Fig. 4(b).

The next weakness of the one-dimensional model (i.e., Eq. (4)) is that the fracture energy is constant regardless of the fracture mode [136]. However, most materials have different fracture energies with respect to the fracture mode [12] and display an anisotropic failure surface [45], as discussed previously. Thus, the model is limited with regards to mixed mode computation, espe-

cially when the mode I fracture energy is different from the mode II fracture energy. Such issues associated with the positive stiffness and the constant fracture energy cannot be tackled through the computational implementation because the fracture energy and the stiffness are an outcome of the traction-separation relationship.

Finally, the effective displacement-based models are unable to demonstrate the difference between the positive normal separation and the negative normal separation because the effective displacement is defined in terms of the square of the normal separation and the square of the tangential separation. Thus, one may need to introduce an additional traction-separation relation for the case of negative normal separation. Otherwise, the model provides the same amount of loss of cohesive traction regardless of the sign of the normal separation.

4 General Potential-Based Models

As shown in the previous section, effective displacement-based cohesive zone models have several limitations. Potential-based models, the emphasis of this review article, have been developed to circumvent some of those limitations. Cohesive traction-separation relationships are created on the basis of a potential, which is a function of normal and tangential separations (Δ_n, Δ_t) instead of the effective displacement ($\bar{\Delta}$). The derivative of a potential with respect to the normal separation leads to the normal cohesive traction while the derivative of a potential with respect to the tangential separation results in the tangential cohesive traction. Notice that the cohesive traction obtained from potential-based models represent monotonic material separation phenomena. If one accounts for additional physical phenomena such as fatigue loading, contact and frictional sliding along fracture surface, oxide formation on fracture surface, etc., one may introduce additional constitutive relationships in conjunction with a potential-based model.

Six general potential-based cohesive zone models are discussed in this paper—see Table 2. The first two models [4,5] are based on polynomial representations—see Sec. 5. The next three models [7–9] are based on the concept of the universal binding energy by Rose et al. [143]—see Sec. 6. In order to address limitations of previous effective and general models, the so-called PPR (Park–Paulino–Roesler) polynomial-based potential was formulated. This model is presented separately in Sec. 7.

5 General Potential-Based Models With Polynomials

This section reviews two potential-based models: one by Needleman [4] and the other by Freed and Banks-Sills [5], both of
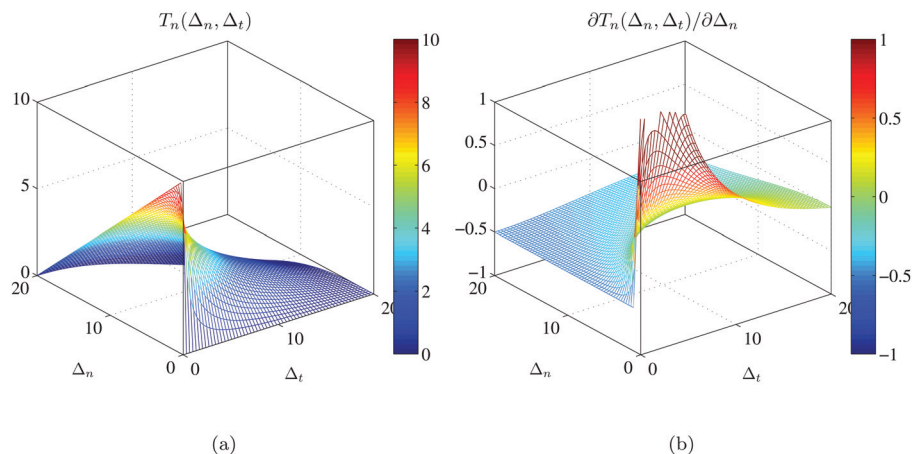

Fig. 4 Effective displacement-based model with a linear softening: (a) normal cohesive traction, and (b) its derivative with respect to the normal separation (Δ_n) for $\bar{T} = \sigma_{max}(1 - \bar{\Delta})$ where $\phi_n = 100$ N/m and $\sigma_{max} = 10$ MPa

Table 2 General potential-based models for cohesive fracture

Potential-based model	Normal interaction	Tangential interaction	Universal binding energy
Needleman, 1987 [4]	Cubic polynomial	Linear	N
Needleman, 1990 [7]	Exponential	Periodic	Y
Beltz and Rice, 1991 [8]	Exponential	Periodic	Y
Xu and Needleman, 1993 [9]	Exponential	Exponential	Y
Freed and Banks-Sills, 2008 [5]	Cubic polynomial	Linear	N
Park, Paulino and Roesler, 2009 [3]	Polynomial	Polynomial	N

which utilize cubic polynomials for the normal cohesive traction and a linear function for the tangential cohesive traction. These models are summarized in Table 2.

5.1 Cubic-Linear Potential-Based Model. An interfacial debonding potential, which defines the constitutive relationship along fracture interfaces, was introduced by Needleman [4] and was utilized to investigate void nucleation and growth [4,148–150]. The potential consists of polynomials formulated in terms of a normal separation (Δ_n) and a tangential separation (Δ_t) along the interface, i.e.,

$$\Psi(\Delta_n, \Delta_t) = \frac{27}{4}\sigma_{\max}\delta_n \left\{ \frac{1}{2}\left(\frac{\Delta_n}{\delta_n}\right)^2 \left[1 - \frac{4}{3}\left(\frac{\Delta_n}{\delta_n}\right) + \frac{1}{2}\left(\frac{\Delta_n}{\delta_n}\right)^2 \right] \right.$$
$$\left. + \frac{1}{2}\alpha_s\left(\frac{\Delta_t}{\delta_n}\right)^2 \left[1 - 2\left(\frac{\Delta_n}{\delta_n}\right) + \left(\frac{\Delta_n}{\delta_n}\right)^2 \right] \right\} \quad (19)$$

where $\sigma_{\max}$ is the maximum traction carried by the interface under the mode I fracture condition, δ_n is a characteristic length, and α_s is a shear stiffness parameter. The interfacial normal and tangential tractions are obtained from the first derivatives of the potential

$$T_n = \frac{\partial \Psi}{\partial \Delta_n} = \frac{27}{4}\sigma_{\max}\left\{ \left(\frac{\Delta_n}{\delta_n}\right)\left[1 - 2\left(\frac{\Delta_n}{\delta_n}\right) + \left(\frac{\Delta_n}{\delta_n}\right)^2 \right] \right.$$
$$\left. + \alpha_s\left(\frac{\Delta_t}{\delta_n}\right)^2 \left[\left(\frac{\Delta_n}{\delta_n}\right) - 1 \right] \right\}$$
$$T_t = \frac{\partial \Psi}{\partial \Delta_t} = \frac{27}{4}\sigma_{\max}\left\{ \alpha_s\left(\frac{\Delta_t}{\delta_n}\right)\left[1 - 2\left(\frac{\Delta_n}{\delta_n}\right) + \left(\frac{\Delta_n}{\delta_n}\right)^2 \right] \right\} \quad (20)$$

when normal separation is smaller than a characteristic length scale ($\Delta_n < \delta_n$). If Δ_n is greater than δ_n, the cohesive interactions are set to zero.

The interfacial normal traction reaches the cohesive strength ($\sigma_{\max}$) when $\Delta_n = \delta_n/3$ and $\Delta_t = 0$. Additionally, the area under the normal traction-separation curve with $\Delta_t = 0$ is equal to the mode I fracture energy (ϕ_n). The mode I fracture energy is related to the characteristic length (δ_n) through the expression

$$\phi_n = 9\sigma_{\max}\delta_n/16 \quad (21)$$

In addition, the higher the shear parameter α_s, the stiffer the response along the tangential direction. Thus, the traction-separation relationship shown in Eq. (20) is mainly associated with mode I fracture properties, i.e., fracture energy and cohesive strength.

Figure 5 illustrates the potential and its gradient with respect to the separations (Δ_n, Δ_t) where $\phi_n = 100$ N/m, $\sigma_{\max} = 30$ MPa, and $\alpha_s = 10$. The normal traction demonstrates elastic behavior from $\Delta_n = 0$ to $\Delta_n = \delta_n/3$, the maximum strength ($\sigma_{\max} = 30$ MPa) at $\Delta_n = \delta_n/3$, and softening behavior from $\Delta_n = \delta_n/3$ to $\Delta_n = \delta_n$. The tangential traction increases linearly without bound as the tangential separation increases. Note that large shear separation should eventually result in weakening of the material behavior. Therefore, the model has limitations if a relatively large shear separation develops [7].

5.2 Revisited Cubic-Linear Potential-Based Model. Following the model by Needleman [4], Freed and Bank-Sills [5] developed a potential-based model with cubic polynomials for the application of bimaterial interfacial fracture. The potential-based model is motivated by the fact that the critical interface energy release rate is a function of mode-mixity or phase angle (θ) [94]. Thus, the potential is derived as a function of an effective displacement ($\widetilde{\Delta}$) and a phase angle. The effective displacement ($\widetilde{\Delta}$) and phase angle (θ) are defined as

$$\widetilde{\Delta} = \sqrt{\Delta_n^2 + \Delta_t^2}, \quad \theta = \tan^{-1}\frac{\Delta_t}{\Delta_n} \quad (22)$$

Freed and Bank-Sills [5] expressed the potential as

$$\Psi(\widetilde{\Delta}, \theta) = \frac{27}{4}t_0^*(\theta)\widetilde{\Delta}\left[\frac{1}{4}\left(\frac{\widetilde{\Delta}}{\delta_c^*(\theta)}\right)^3 - \frac{2}{3}\left(\frac{\widetilde{\Delta}}{\delta_c^*(\theta)}\right)^2 + \frac{1}{2}\left(\frac{\widetilde{\Delta}}{\delta_c^*(\theta)}\right)\right] \quad (23)$$

for $\widetilde{\Delta} \leq \delta_c^*(\theta)$, where δ_c^* and t_0^* are given as

$$\delta_c^*(\theta) = \delta_n\sqrt{1 + \tan^2\theta}, \quad t_0^*(\theta) = \sigma_{\max}\sqrt{1 + \tan^2\theta} \quad (24)$$

If $\widetilde{\Delta}$ is greater than $\delta_c^*(\theta)$, the cohesive tractions are set to zero. Note that $t_0^*(\theta)$ varies from $\sigma_{\max}$ to infinity, and thus the potential is unbounded when $\theta = \pi/2$.

Alternatively, the potential of Eq. (23) can be expressed in terms of Δ_n and Δ_t by substituting the effective displacement and the phase angle (Eq. (22)) into the original potential expression (Eq. (23)), which is given as

$$\Psi(\Delta_n, \Delta_t) = \frac{27}{4}\sigma_{\max}\frac{\Delta_n^2 + \Delta_t^2}{\delta_n}\left[\frac{1}{4}\left(\frac{\Delta_n}{\delta_n}\right)^2 - \frac{2}{3}\left(\frac{\Delta_n}{\delta_n}\right) + \frac{1}{2}\right] \quad (25)$$

Thus, the potential by Freed and Banks-Sills [5] is similar to the earlier potential by Needleman [4]; cf. Eq. (25) and Eq. (19). Note that both potentials are the same when Δ_t is zero (i.e., mode I case), and that they are quadratic with respect to the tangential separation. The normal and tangential cohesive tractions of the model by Freed–Banks-Sills [5] are given as

$$T_n = \frac{27}{4}\sigma_{\max}\left\{ \left(\frac{\Delta_n}{\delta_n}\right)\left[\left(\frac{\Delta_n}{\delta_n}\right)^2 - 2\left(\frac{\Delta_n}{\delta_n}\right) + 1\right]\right.$$
$$\left. + \frac{1}{2}\left(\frac{\Delta_t}{\delta_n}\right)^2\left[\left(\frac{\Delta_n}{\delta_n}\right) - \frac{4}{3}\right] \right\}$$
$$T_t = \frac{27}{4}\sigma_{\max}\left\{ \frac{2\Delta_t}{\delta_n}\left[\frac{1}{4}\left(\frac{\Delta_n}{\delta_n}\right)^2 - \frac{2}{3}\left(\frac{\Delta_n}{\delta_n}\right) + \frac{1}{2}\right] \right\} \quad (26)$$
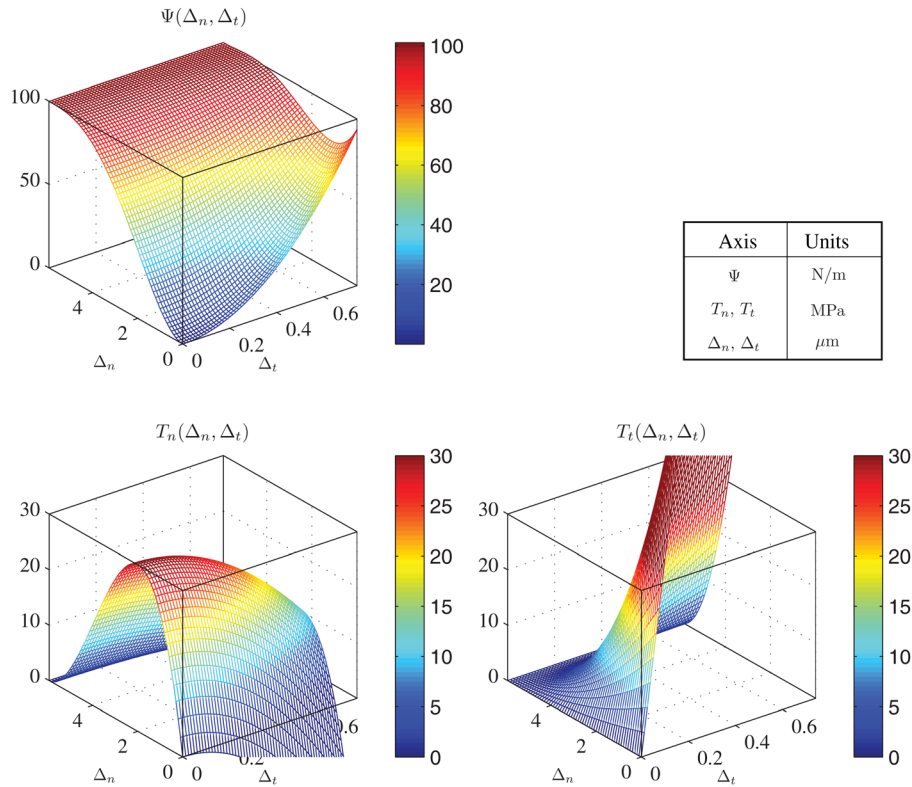
Fig. 5 Needleman [4] potential (Ψ) and its gradients (T_n, T_t) with respect to displacement separations (Δ_n, Δ_t); $\phi_n = 100$ N/m, $\sigma_{max} = 30$ MPa, and $\alpha_s = 10$. The gradients refer to a cubic-linear model.

when $\widetilde{\Delta}$ is smaller than $\delta_c^*(\theta)$. Similarly to the model by Needleman [4], the normal cohesive traction consists of cubic polynomials with respect to the normal separation, while the tangential cohesive traction is linear with respect to the tangential separation. The characteristic length scale (δ_n) is obtained from $\delta_n = 16\phi_n/9\sigma_{max}$, which corresponds to Eq. (21) of Needleman's model [4]. The potential and its gradient are plotted in Fig. 6 with $\phi_n = 100$ N/m and $\sigma_{max} = 30$ MPa. The normal traction reaches the cohesive strength when $\Delta_n = \delta_n/3$ and $\Delta_t = 0$, while the tangential traction is unbounded (no softening occurs), as in the model by Needleman [4].

6 General Potential-Based Models With Universal Binding Energy

Rose et al. [143] proposed an atomistic potential, which provides the relationship between metallic binding energies and lattice parameters. The potential, called the universal binding energy, is defined as

$$\Psi = -(1 + \ell)\exp(-\ell) \qquad (27)$$

where ℓ is the scaled separation associated with the Thomas–Fermi screening length. The universal binding energy has been extensively utilized to represent the work of interfacial separation [6–9,98,151]. For instance, Rice and Wang [151] limited their investigation to large tangential separation and obtained the normal traction-separation relationship on the basis of the derivative of the potential given by Eq. (27),

$$T_n(\Delta_n) = E_0 \left(\frac{\Delta_n}{\delta_n}\right)\exp\left(-\alpha_n\frac{\Delta_n}{\delta_n}\right) \qquad (28)$$

where E_0 is the initial modulus for one-dimensional tensile straining of the interface layer, and the parameters δ_n and α_n are

associated with the fracture energy and the cohesive strength. Needleman [6] utilized the exponential potential of Eq. (27) with linear shear interaction, and obtained the following expression:

$$\Psi(\Delta_n, \Delta_t) = \frac{9}{16}\sigma_{max}\delta_n\left\{1 - \left[1 + \frac{z\Delta_n}{\delta_n} - \frac{1}{2}\alpha_s\left(\frac{z\Delta_t}{\delta_n}\right)^2\right]\exp\left(-\frac{z\Delta_n}{\delta_n}\right)\right\} \qquad (29)$$

where $z = 16e/9$ and $e = \exp(1)$. Notice that the potential includes the term that agrees with the universal binding energy, i.e., $-(1 + z\Delta_n/\delta_n)\exp(-z\Delta_n/\delta_n)$, and that the tangential traction ($T_t = \partial\Psi/\partial\Delta_t$) is linear with respect to tangential separation, as it was in the previous model by Needleman [4]; see Sec. 5. Ortiz and Pandolfi [98] utilized the exponential expression for the one-dimensional traction potential model based on the effective displacement, as discussed in Sec. 3 (Eq. (8)). Furthermore, Needleman [7] created an exponential-periodic potential, which is a function of normal and tangential separations. Later, the exponential-periodic potential was generalized by Beltz and Rice [8]. The normal interaction has the exponential expression based on the universal binding energy [143], while the tangential interaction employs the periodic function due to the periodic dependence of the underlying lattice [152]. In order to consider the complete shear failure, the exponential-exponential potential was formulated by Xu and Needleman [9]. The following subsections review three exponential potential-based cohesive models: the exponential-periodic model [7], the generalized exponential-periodic model [8], and the exponential-exponential model [9,96].

6.1 Exponential-Periodic Potential-Based Model. The exponential–periodic potential by Needleman [7] accommodates a large shear displacement jump—cf. Figs. 7 and 5. An exponential expression was utilized for the normal traction-separation relationship to resemble the universal binding energy (Eq. (27)). A
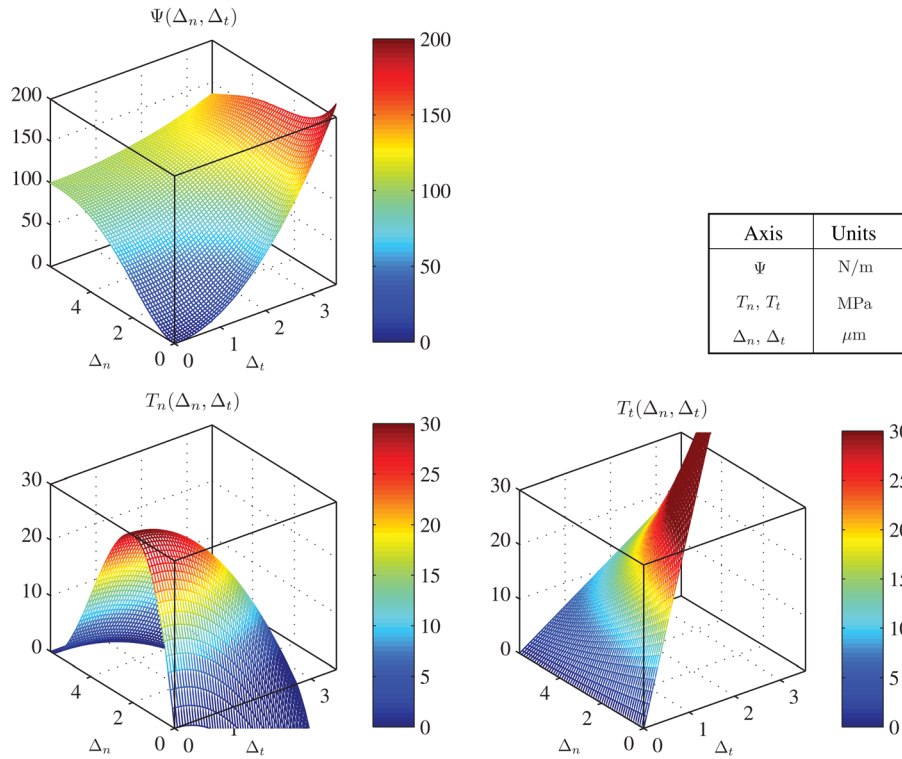
Fig. 6 Freed and Banks-Sills [5] potential (Ψ) and its gradients (T_n, T_t) with respect to displacement separations (Δ_n, Δ_t); $\phi_n = 100$ N/m, and $\sigma_{max} = 30$ MPa. The gradients refer to a revisited cubic-linear model.
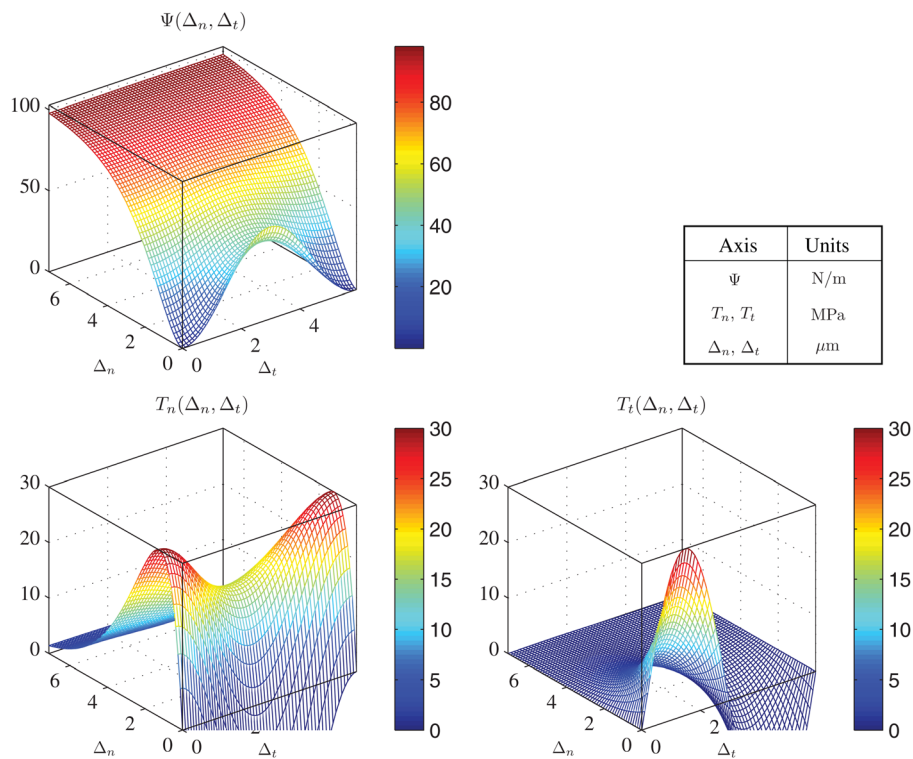

Fig. 7 Needleman [7] exponential-periodic potential and its gradients; $\phi_n = 100$ N/m, and $\sigma_{max} = 30$ MPa

periodic expression was employed for the tangential traction-separation relationship because of the periodic dependence of the underlying lattice. The exponential-periodic potential is given by

$$\Psi(\Delta_n, \Delta_t) = \frac{\sigma_{\max} e \delta_n}{z} \left\{ 1 - \left[1 + \frac{z\Delta_n}{\delta_n} - \beta_s z^2 \left[1 - \cos\left(\frac{2\pi\Delta_t}{\delta_t}\right) \right] \right] \right.$$
$$\left. \times \exp\left(-\frac{z\Delta_n}{\delta_n}\right) \right\} \tag{30}$$

where $z = 16e/9$, and β_s is a nondimensional constant. The derivative of the potential leads to the normal and tangential cohesive tractions,

$$T_n = \sigma_{\max} e \left\{ \frac{z\Delta_n}{\delta_n} - \beta_s z^2 \left[1 - \cos\left(\frac{2\pi\Delta_t}{\delta_t}\right) \right] \right\} \exp\left(-\frac{z\Delta_n}{\delta_n}\right)$$

$$T_t = \sigma_{\max} e \left\{ 2\pi\beta_s z \left(\frac{\delta_n}{\delta_t}\right) \sin\left(\frac{2\pi\Delta_t}{\delta_t}\right) \right\} \exp\left(-\frac{z\Delta_n}{\delta_n}\right) \tag{31}$$

The normal cohesive strength, $\sigma_{\max}$, is attained when $\Delta_n = \delta_n/z$ and $\Delta_t = 0$. Additionally, the characteristic length, δ_n, is evaluated by its association with the mode I fracture energy and cohesive strength, i.e.,

$$\phi_n = \sigma_{\max} e \delta_n / z \tag{32}$$

The other characteristic length, δ_t, is assumed to be the same as δ_n, and the nondimensional scalar parameter, β_s, is calibrated ($\beta_s = 1/2\pi ez$) so that the maximum value of T_t with $\Delta_n = 0$ is the same as $\sigma_{\max}$.

The potential and the traction-separation relationships are plotted in Fig. 7 where $\phi_n = 100$ N/m and $\sigma_{\max} = 30$ MPa. The normal traction demonstrates exponential softening behavior, while the tangential traction illustrates periodic behavior. However, the imposed fracture properties are based solely on the mode I fracture parameters, i.e., the fracture energy (ϕ_n) and the cohesive strength ($\sigma_{\max}$), even though the potential considers mixed-mode cohesive fracture interaction. The exponential-periodic potential-based model does not include mode II fracture parameters and, therefore, is limited in its ability to describe general mixed-mode fracture behavior.

6.2 Generalized Exponential-Periodic Potential-Based Model. The exponential-periodic potential proposed by Needleman [7] was generalized by Beltz and Rice [8,153]. They investigated the competition between cleavage decohesion and dislocation nucleation for a slip plane under general loading. For a broader perspective, cleavage decohesion could be considered as normal separation while regarding dislocation as tangential separation. Similarly to the potential proposed by Needleman [7], the normal traction $T_n(\Delta_n, \Delta_t)$ is given by the following exponential function,

$$T_n = [B(\Delta_t)\Delta_n - C(\Delta_t)] \exp(-\Delta_n/\delta_n) \tag{33}$$

while the tangential traction $T_t(\Delta_n, \Delta_t)$ is defined as a periodic function, based on the Peierls concept [152,154], i.e.,

$$T_t = A(\Delta_n) \sin\left(\frac{2\pi\Delta_t}{\delta_t}\right) \tag{34}$$

where $A(\Delta_n)$, $B(\Delta_t)$, and $C(\Delta_t)$ are functions chosen to satisfy the following boundary conditions. First, note that the potential is an exact differential which satisfies the symmetry condition of Eq. (7). Second, because the normal traction (Eq. (33)) is zero when normal and tangential displacements are zero (i.e., initial condition), $C(0)$ is equal to zero, i.e.,

$$C(0) = 0 \tag{35}$$

As the area under a cohesive interaction represents the fracture energy, the normal traction of a cleavage fracture is associated with the surface energy, γ_s,

$$\int_0^\infty T_n(\Delta_n, 0) d\Delta_n = 2\gamma_s = \phi_n \tag{36}$$

In addition, the tangential traction of a dislocation nucleation procedure is related to the unstable stacking energy, γ_{us},

$$\int_0^{\delta_t/2} T_t(0, \Delta_t) d\Delta_t = \gamma_{us} = \phi_t \tag{37}$$

which can be made equivalent to the mode II fracture energy (ϕ_t) in macroscopic fracture. The normal and tangential tractions (T_n and T_t) satisfy the boundary conditions at the complete normal separation ($\Delta_n = \infty$), i.e.,

$$T_n(\infty, \Delta_t) = 0, \quad T_t(\infty, \Delta_t) = 0 \tag{38}$$

because fracture surfaces cannot transfer tractions when complete separation occurs along the normal direction. Note that boundary conditions associated with the complete shear separation are not introduced. Although the tangential traction is set to be zero when Δ_t is equal to $\delta_t/2$, i.e., $T_t(\Delta_n, \delta_t/2) = 0$; the normal traction is not necessarily zero, e.g., $T_n(\Delta_n, \delta_t/2) \neq 0$. Because of this fact, Beltz and Rice [8] introduced an additional length scale parameter, Δ_n^*, which satisfies the following condition:

$$T_n(\Delta_n^*, \delta_t/2) = 0 \tag{39}$$

From Eqs. (7), (35)–(39), the general expression for $A(\Delta_n)$, $B(\Delta_t)$, and $C(\Delta_t)$ are obtained as

$$A(\Delta_n) = \frac{\pi\gamma_{us}}{\delta_t} - \frac{2\pi\gamma_s}{\delta_t} \left\{ q\left[1 - \exp\left(-\frac{\Delta_n}{\delta_n}\right) \right] \right.$$
$$\left. - \left(\frac{q-r}{1-r}\right) \frac{\Delta_n}{\delta_n} \exp\left(-\frac{\Delta_n}{\delta_n}\right) \right\}$$
$$B(\Delta_t) = \frac{2\gamma_s}{\delta_n^2} \left\{ 1 - \left(\frac{q-r}{1-r}\right) \sin^2\left(\frac{\pi\Delta_t}{\delta_t}\right) \right\}$$
$$C(\Delta_t) = \frac{2\gamma_s}{\delta_n} \frac{r(1-q)}{1-r} \sin^2\left(\frac{\pi\Delta_t}{\delta_t}\right) \tag{40}$$

with

$$q = \frac{\gamma_{us}}{2\gamma_s} = \frac{\phi_t}{\phi_n}, \quad r = \frac{\Delta_n^*}{\delta_n} \tag{41}$$

where δ_n, δ_t, and Δ_n^* are length scale parameters. Substitution of Eq. (40) into Eq. (33) and Eq. (34), and integration of Eq. (33) and Eq. (34) lead to the generalized exponential-periodic potential of Beltz and Rice [8,153]

$$\Psi = 2\gamma_s + 2\gamma_s \exp\left(-\frac{\Delta_n}{\delta_n}\right) \left\{ \left[q + \left(\frac{q-r}{1-r}\right) \frac{\Delta_n}{\delta_n} \right] \sin^2\left(\frac{\pi\Delta_t}{\delta_t}\right) \right.$$
$$\left. - \left[1 + \frac{\Delta_n}{\delta_n} \right] \right\} \tag{42}$$

The characteristic length parameters (δ_n, δ_t) are determined through their association with the cohesive strengths ($\sigma_{\max}$, $\tau_{\max}$) and the fracture energies (ϕ_n, ϕ_t), i.e.,
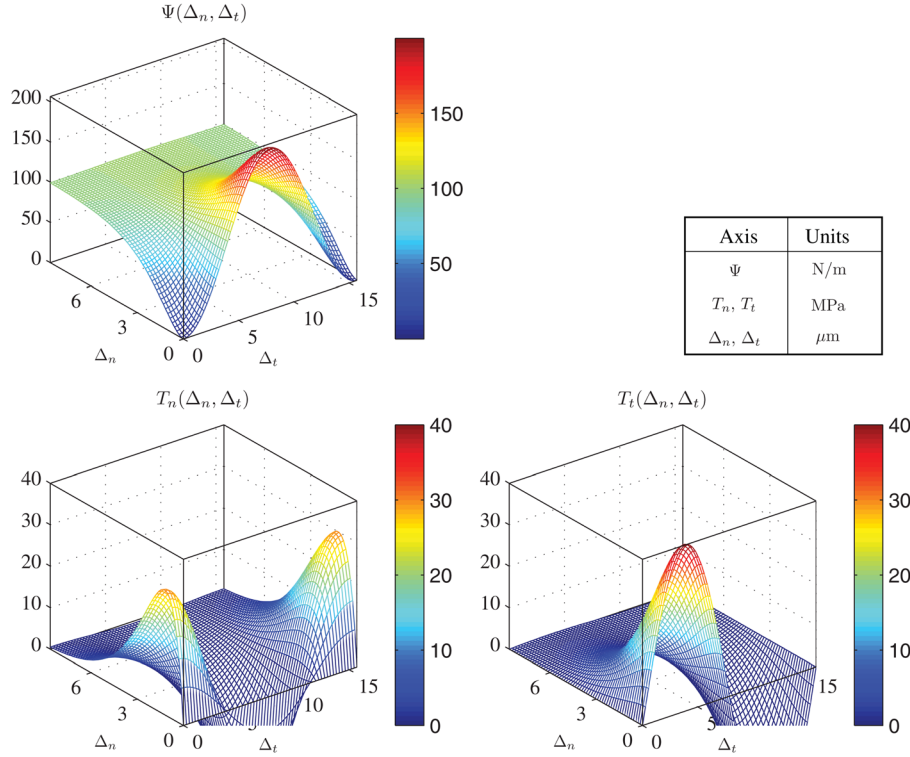
Fig. 8 Beltz and Rice [8] generalized exponential-periodic potential and its gradients; $\phi_n = 2\gamma_s = 100$ N/m, $\phi_t = \gamma_{us} = 200$ N/m, $\sigma_{max} = 30$ MPa, $\tau_{max} = 40$ MPa, and $r = 0$

Axis	Units
Ψ	N/m
T_n, T_t	MPa
Δ_n, Δ_t	μm

$$\delta_n = \phi_n/(e\sigma_{max}), \quad \delta_t = \pi\phi_t/\tau_{max} \tag{43}$$

The other length scale parameter Δ_n^* is defined by Beltz and Rice [8] as follows:

"Δ_n^* is the value of Δ_n after shearing to the state $\Delta_t = \delta_t/2$ under conditions of zero tension, $T_n = 0$, (i.e., relaxed shearing)."

Note that the parameter r, associated with a length scale Δ_n^*, was estimated by using embedded atom methods [155].

Figure 8 demonstrates the potential function and its traction-separation relationships where $\phi_n = 2\gamma_s = 100$ N/m, $\phi_t = \gamma_{us} = 200$ N/m, $\sigma_{max} = 30$ MPa, $\tau_{max} = 40$ MPa, and $r = 0$. However, the potential contains a length scale fracture parameter, Δ_n^*, which is difficult to evaluate. Furthermore, the potential cannot be utilized for general interfacial shear failure because the periodic function is employed for dislocation nucleation along the tangential direction.

6.3 Exponential-Exponential Potential-Based Model. In order to characterize complete interfacial shear failure, Xu and Needleman [9] employed the exponential expression for the tangential traction rather than the periodic function. The exponential-exponential potential is expressed as

$$\Psi(\Delta_n, \Delta_t) = \phi_n + \phi_n \exp\left(\frac{-\Delta_n}{\delta_n}\right)\left\{\left[1 - r + \frac{\Delta_n}{\delta_n}\right]\frac{(1-q)}{(r-1)}\right.$$
$$\left. - \left[q + \frac{(r-q)}{(r-1)}\frac{\Delta_n}{\delta_n}\right]\exp\left(-\frac{\Delta_t^2}{\delta_t^2}\right)\right\} \tag{44}$$

The first derivative of the exponential-exponential potential results in the interfacial cohesive tractions,

$$T_n = \frac{\phi_n}{\delta_n}\exp\left(\frac{-\Delta_n}{\delta_n}\right)\left\{\frac{\Delta_n}{\delta_n}\exp\left(-\frac{\Delta_t^2}{\delta_t^2}\right)\right.$$
$$\left. + \frac{(1-q)}{(r-1)}\left[1 - \exp\left(-\frac{\Delta_t^2}{\delta_t^2}\right)\right]\left[r - \frac{\Delta_n}{\delta_n}\right]\right\}$$
$$T_t = \frac{\phi_n}{\delta_n}\frac{2\delta_n}{\delta_t}\frac{\Delta_t}{\delta_t}\left[q + \frac{(r-q)}{(r-1)}\frac{\Delta_n}{\delta_n}\right]\exp\left(\frac{-\Delta_n}{\delta_n}\right)\exp\left(-\frac{\Delta_t^2}{\delta_t^2}\right) \tag{45}$$

Similar to the generalized exponential-periodic potential [8], the two length scale parameters (δ_n, δ_t) are evaluated by relating the fracture energies (ϕ_n, ϕ_t) to the cohesive strength $(\sigma_{max}, \tau_{max})$, i.e.,

$$\phi_n = \sigma_{max}e\delta_n, \quad \phi_t = \sqrt{e/2}\tau_{max}\delta_t \tag{46}$$

The nondimensional parameter q is the ratio of the mode II fracture energy (ϕ_t) to the mode I fracture energy (ϕ_n), i.e.,

$$q = \phi_t/\phi_n \tag{47}$$

The nondimensional parameter r is defined as

$$r = \Delta_n^*/\delta_n \tag{48}$$

where Xu and Needleman [9,96] indicate that

"Δ_n^* is the value of Δ_n after complete shear separation under the condition of zero normal tension, i.e., $T_n = 0$."

Note that when the mode I fracture energy is the same as the mode II fracture energy $(q = 1)$, the effect of the parameter r (or Δ_n^*) disappears, and the potential is simplified as

$$\Psi(\Delta_n, \Delta_t) = \phi_n - \phi_n\left[1 + \frac{\Delta_n}{\delta_n}\right]\exp\left(\frac{-\Delta_n}{\delta_n}\right)\exp\left(-\frac{\Delta_t^2}{\delta_t^2}\right) \tag{49}$$
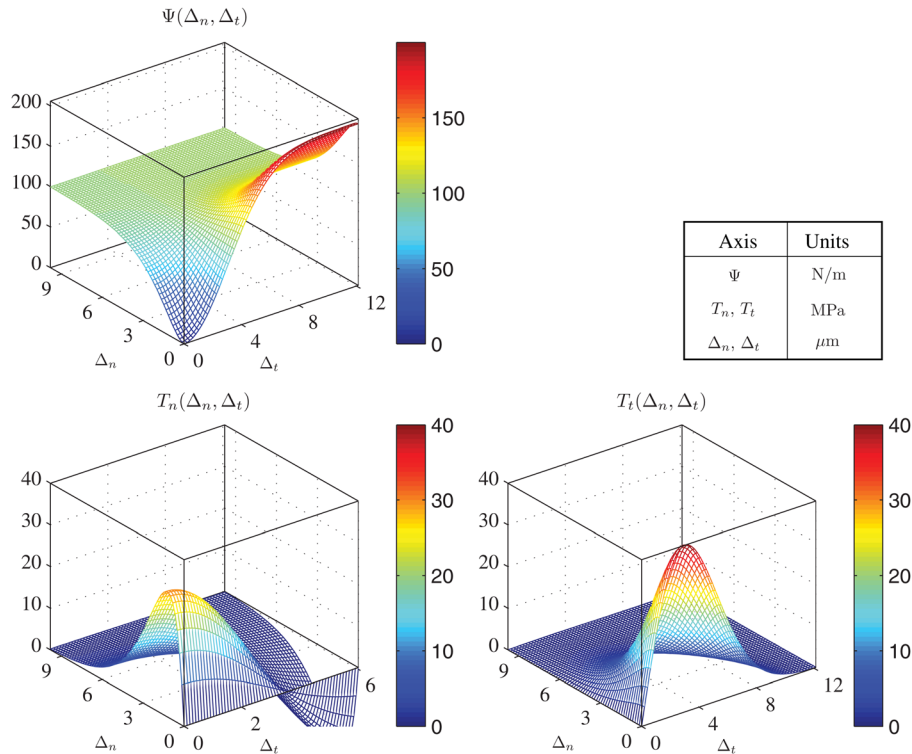
Fig. 9 Xu and Needleman [9] exponential-exponential potential and its gradients; $\phi_n = 100$ N/m, $\phi_t = 200$ N/m, $\sigma_{max} = 30$ MPa, $\tau_{max} = 40$ MPa, and $r = 0$

The exponential-exponential potential and its interfacial cohesive responses are plotted in Fig. 9. The normal and tangential tractions not only demonstrate the exponentially decreasing softening but represent the different fracture parameters, i.e., fracture energy ($\phi_n = 100$ N/m, $\phi_t = 200$ N/m) and cohesive strength ($\sigma_{max} = 30$ MPa, $\tau_{max} = 40$ MPa), in mode I and mode II.

6.4 Remarks on the Exponential-Exponential Model. The exponential-exponential potential by Xu and Needleman [9] has been extensively utilized to investigate various crack growth phenomena in brittle solids [96,156], particle/matrix interfaces [157], elastic-viscoplastic solids [158], steel-PMMA interfaces [159], alumina/titanium composites [160], etc. However, the model has several limitations arising from the fracture boundary conditions and the exponential expression. First, a complete tangential failure condition is not introduced along the normal cohesive traction, which leads to an inconsistent boundary condition. Because of such a boundary condition, the additional length scale parameter (Δ_n^*) is introduced, and thus the model may provide nonphysical cohesive interactions for several cases (i.e., $r \neq 0$, $q \neq 1$). Notice that the exponential-exponential potential is derived by applying the same boundary conditions as the exponential-periodic potential derived by Beltz and Rice [8]. The boundary conditions associated with cohesive fracture are summarized as follows:

- mode I fracture energy: $\int_0^\infty T_n(\Delta_n, 0) d\Delta_n = \phi_n$
- mode II fracture energy: $\int_0^\infty T_t(0, \Delta_t) d\Delta_t = \phi_t$
- complete normal failure for the infinite normal separation: $T_n(\infty, \Delta_t) = 0$
- complete tangential failure for the infinite normal separation: $T_t(\infty, \Delta_t) = 0$
- complete tangential failure for the infinite shear separation: $T_t(\Delta_n, \infty) = 0$

The main difference between the generalized exponential-periodic potential of Beltz and Rice [8] and the exponential-

exponential potential of Xu and Needleman [9] is that $\Delta_t = \delta_t/2$ in the exponential-periodic potential may not be a sufficient condition for complete failure along the normal direction, while the infinite tangential separation ($\Delta_t = \infty$) in the exponential-exponential potential can be a sufficient condition for the complete failure along the normal and tangential directions. In a strict sense, when tangential separation reaches infinity ($\Delta_t = \infty$), the boundary condition for the complete normal failure, i.e., $T_n(\Delta_n, \infty) = 0$, should be introduced in the exponential-exponential potential, which would result in consistent boundary conditions.

However, instead of enforcing the boundary condition $T_n(\Delta_n, \infty) = 0$, the alternative boundary condition, $T_n(\Delta_n^*, \infty) = 0$, is utilized by introducing the additional length scale parameter Δ_n^*, as discussed previously. The length scale parameter Δ_n^* (or nondimensional parameter r) is difficult to calculate based on either physical experiments or explanations.

Because of the deficiency in the boundary condition of complete normal failure (the inconsistent boundary condition), when the mode I fracture energy is greater than mode II fracture energy, the cohesive interactions do not correspond to physical fracture behavior. Figure 10 illustrates that the potential provides unacceptably high normal traction around ($\Delta_n \approx 5\mu$m, $\Delta_t \gg 0$) although almost complete tangential failure occurs around that region. The normal traction does not decrease with respect to increasing tangential separation, $T_n(\Delta_n, \infty) \neq 0$, although the increase of the tangential separation weakens materials and results in the decrease of the normal traction. Additionally, when the mode I fracture energy is different from the mode II fracture energy, the model displays inconsistent variation of the work-of-separation with respect to mode-mixity [3,161]. However, when the mode I fracture energy is the same as the mode II fracture energy ($\phi_n = \phi_t$), the boundary condition associated with the complete normal failure is satisfied, i.e., $T_n(\Delta_n, \infty) = 0$, as illustrated in Fig. 11.

Additionally, the exponential-exponential potential originates from the atomistic potential which includes both elastic and failure behavior. When cohesive surface elements are inserted in a
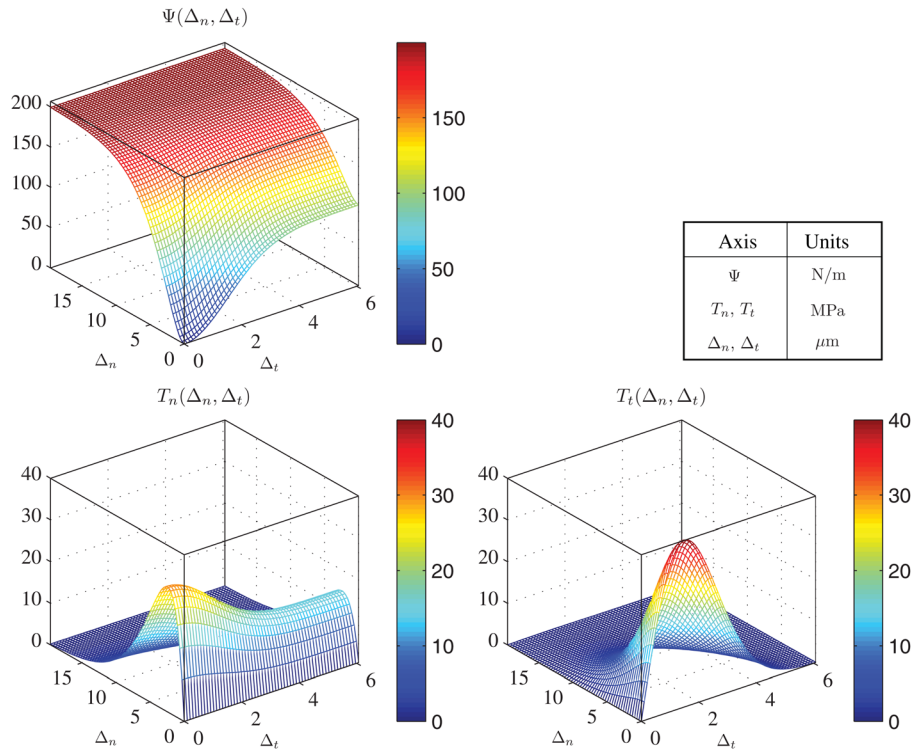
Fig. 10 Xu and Needleman [9] exponential-exponential potential and its gradients; $\phi_n = 200$ N/m, $\phi_t = 100$ N/m, $\sigma_{max} = 30$ MPa, $\tau_{max} = 40$ MPa, and $r = 0$
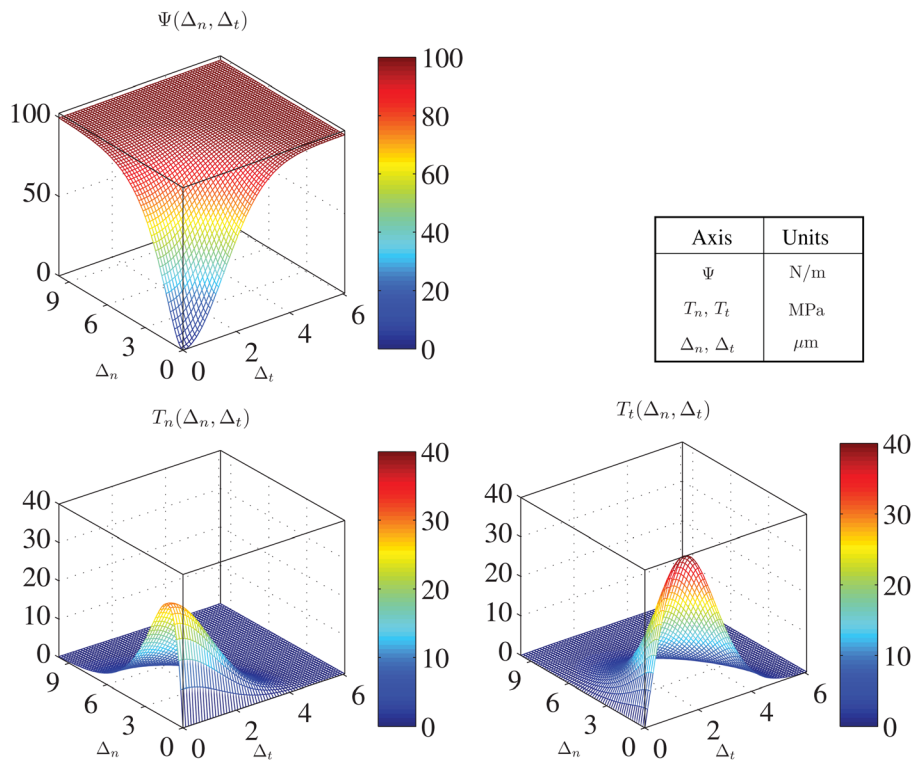

Fig. 11 Xu and Needleman [9] exponential-exponential potential and its gradients; $\phi_n = 100$ N/m, $\phi_t = 100$ N/m, $\sigma_{max} = 30$ MPa, and $\tau_{max} = 40$ MPa

large domain, numerical simulations of the cohesive zone model can lead to large artificial compliance [144,162]. Ideally, the elastic behavior should generally be eliminated in the numerical implementation of cohesive surface elements. Moreover, because of the exponential expression, the traction free condition occurs when separation is infinite, although a final crack opening width is finite in macroscopic scale fracture. Note that the final crack opening width is separation, which provides complete failure condition.

The limitations of the exponential-exponential potential-based model are summarized as follows:

- It contains an ill-defined fracture parameter, Δ_n^*, which is difficult to determine experimentally. However, the parameter disappears when the mode I fracture energy is the same as the mode II fracture energy (see Fig. 11).
- It may not be applicable when the mode I fracture energy is different from the mode II fracture energy.
- It provides large artificial compliance for numerical simulation of cohesive surface elements because it does not allow any control of the elastic behavior.
- Due to the exponential function, the final crack opening width is infinite, which does not resemble macroscopic fracture behavior.

Notice that one may be able to control the initial slope (or artificial compliance) and change the shape of the traction-separation relationship through introducing additional fracture parameters in the exponential-exponential model. However, the other limitations, i.e., ill-defined fracture parameters, different fracture energies and inconsistent work-of-separation, are not related to the number of fracture parameters, but associated with the complete failure boundary condition, i.e., $T_n(\Delta_n^*, \infty) = 0$.

7 PPR: General Unified Potential-Based Model

In order to tackle limitations in the previous potential-based models, a polynomial-based potential was formulated in conjunction with physical fracture parameters and consistent fracture boundary conditions [3]. Four physical fracture parameters are employed in each fracture mode: fracture energy, cohesive strength, shape, and initial slope. The potential-based model satisfies the following boundary conditions associated with cohesive fracture:

- complete normal failure when $T_n(\delta_n, \Delta_t) = 0$ or $T_n(\Delta_n, \bar{\delta}_t) = 0$
- complete tangential failure when $T_t(\Delta_n, \delta_t) = 0$ or $T_t(\bar{\delta}_n, \Delta_t) = 0$
- mode I fracture energy: $\int_0^{\delta_n} T_n(\Delta_n, 0)d\Delta_n = \phi_n$
- mode II fracture energy: $\int_0^{\delta_t} T_t(0, \Delta_t)d\Delta_t = \phi_t$
- normal cohesive strength: $T_n(\delta_{nc}, 0) = \sigma_{\max}$ where $\frac{\partial T_n}{\partial \Delta_n}\big|_{\Delta_n = \delta_{nc}} = 0$
- tangential cohesive strength: $T_t(0, \delta_{tc}) = \tau_{\max}$ where $\frac{\partial T_t}{\partial \Delta_t}\big|_{\Delta_t = \delta_{tc}} = 0$

In addition to the boundary conditions, shape parameters (α, β) are introduced to characterize various material softening responses, e.g., brittle, plateau and quasi-brittle.

Based on the above boundary conditions, the potential of mixed-mode cohesive fracture, called the PPR potential, is expressed as [3]

$$\Psi(\Delta_n, \Delta_t) = \min(\phi_n, \phi_t) + \left[\Gamma_n\left(1 - \frac{\Delta_n}{\delta_n}\right)^\alpha \left(\frac{m}{\alpha} + \frac{\Delta_n}{\delta_n}\right)^m + \langle \phi_n - \phi_t \rangle\right]$$

$$\times \left[\Gamma_t\left(1 - \frac{|\Delta_t|}{\delta_t}\right)^\beta \left(\frac{n}{\beta} + \frac{|\Delta_t|}{\delta_t}\right)^n + \langle \phi_t - \phi_n \rangle\right] \quad (50)$$

where $\langle \cdot \rangle$ is the Macaulay bracket, i.e.,

$$\langle x \rangle = \begin{cases} 0, & (x < 0) \\ x, & (x \geq 0) \end{cases} \quad (51)$$

The gradient of the PPR potential leads directly to the traction vector,

$$T_n(\Delta_n, \Delta_t) = \frac{\Gamma_n}{\delta_n}\left[m\left(1 - \frac{\Delta_n}{\delta_n}\right)^\alpha \left(\frac{m}{\alpha} + \frac{\Delta_n}{\delta_n}\right)^{m-1}\right.$$

$$\left. - \alpha\left(1 - \frac{\Delta_n}{\delta_n}\right)^{\alpha-1}\left(\frac{m}{\alpha} + \frac{\Delta_n}{\delta_n}\right)^m\right]$$

$$\times \left[\Gamma_t\left(1 - \frac{|\Delta_t|}{\delta_t}\right)^\beta \left(\frac{n}{\beta} + \frac{|\Delta_t|}{\delta_t}\right)^n + \langle \phi_t - \phi_n \rangle\right]$$

$$T_t(\Delta_n, \Delta_t) = \frac{\Gamma_t}{\delta_t}\left[n\left(1 - \frac{|\Delta_t|}{\delta_t}\right)^\beta \left(\frac{n}{\beta} + \frac{|\Delta_t|}{\delta_t}\right)^{n-1}\right.$$

$$\left. - \beta\left(1 - \frac{|\Delta_t|}{\delta_t}\right)^{\beta-1}\left(\frac{n}{\beta} + \frac{|\Delta_t|}{\delta_t}\right)^n\right]$$

$$\times \left[\Gamma_n\left(1 - \frac{\Delta_n}{\delta_n}\right)^\alpha \left(\frac{m}{\alpha} + \frac{\Delta_n}{\delta_n}\right)^m + \langle \phi_n - \phi_t \rangle\right]\frac{\Delta_t}{|\Delta_t|}$$

$$(52)$$

Notice that the value of $T_t(\Delta_n, \Delta_t)$ at $\Delta_t = 0$ exists in the limit sense, i.e.,

$$\lim_{\Delta_t \to 0^+} T_t(\Delta_n, \Delta_t) = 0, \quad \lim_{\Delta_t \to 0^-} T_t(\Delta_n, \Delta_t) = 0 \quad (53)$$

The normal and tangential tractions are defined within the cohesive interaction (softening) region where the fracture surface transfers cohesive normal and tangential tractions—see Sec. 7.1.

The characteristic parameters $(\delta_n, \delta_t; \Gamma_n, \Gamma_t; m, n; \alpha, \beta)$ in the potential function are determined by satisfying the aforementioned boundary conditions. The normal and tangential final crack opening widths (δ_n, δ_t) are expressed as

$$\delta_n = \frac{\phi_n}{\sigma_{\max}}\alpha\lambda_n(1 - \lambda_n)^{\alpha-1}\left(\frac{\alpha}{m} + 1\right)\left(\frac{\alpha}{m}\lambda_n + 1\right)^{m-1}$$

$$\delta_t = \frac{\phi_t}{\tau_{\max}}\beta\lambda_t(1 - \lambda_t)^{\beta-1}\left(\frac{\beta}{n} + 1\right)\left(\frac{\beta}{n}\lambda_t + 1\right)^{n-1} \quad (54)$$

which are characteristic lengths. The energy constants, Γ_n and Γ_t, are given as

$$\Gamma_n = (-\phi_n)^{\frac{\langle \phi_n - \phi_t \rangle}{\phi_n - \phi_t}}\left(\frac{\alpha}{m}\right)^m, \quad \Gamma_t = (-\phi_t)^{\frac{\langle \phi_t - \phi_n \rangle}{\phi_t - \phi_n}}\left(\frac{\beta}{n}\right)^n \quad \text{for} \quad (\phi_n \neq \phi_t)$$

$$(55)$$

and

$$\Gamma_n = -\phi_n\left(\frac{\alpha}{m}\right)^m, \quad \Gamma_t = \left(\frac{\beta}{n}\right)^n \quad \text{for} \quad (\phi_n = \phi_t) \quad (56)$$

The nondimensional exponents, m and n, are expressed as

$$m = \frac{\alpha(\alpha - 1)\lambda_n^2}{(1 - \alpha\lambda_n^2)}, \quad n = \frac{\beta(\beta - 1)\lambda_t^2}{(1 - \beta\lambda_t^2)} \quad (57)$$

where the initial slope indicators (λ_n, λ_t) are the ratio of the critical crack opening width $(\delta_{nc}, \delta_{tc})$ to the final crack opening width, i.e., $\lambda_n = \delta_{nc}/\delta_n$ and $\lambda_t = \delta_{tc}/\delta_t$. Note that the initial slope indicators control elastic behavior. A smaller value of the initial slope indicator provides higher initial stiffness in the traction-separation relationship.

The nondimensional shape parameters (α, β) provide flexibility in the choice of softening shape. This is because the specific shape of the cohesive zone model can significantly affect results of fracture analyses [163–165], especially for quasi-static problems. If the shape parameter indices are equal to two $(\alpha = \beta = 2)$, the resulting gradient of the potential represents an almost linearly
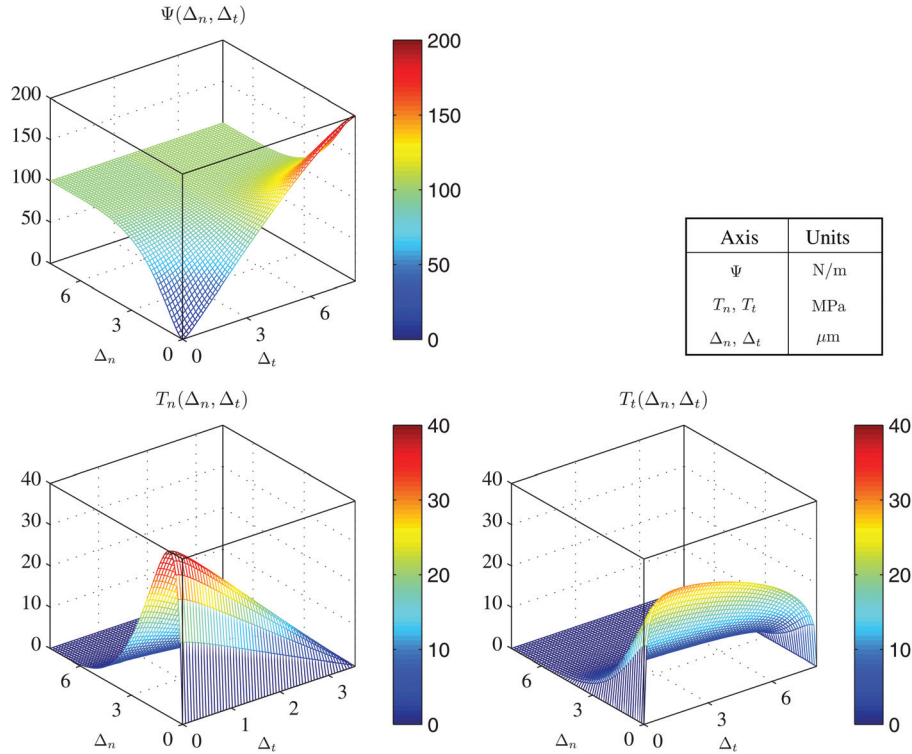
Fig. 12 Unified mixed-mode potential (PPR) [3] and its gradients for the intrinsic cohesive zone model with $\phi_n = 100$ N/m, $\phi_t = 200$ N/m, $\sigma_{\max} = 40$ MPa, $\tau_{\max} = 30$ MPa, $\alpha = 5$, $\beta = 1.3$, $\lambda_n = 0.1$, and $\lambda_t = 0.2$

decreasing cohesive relationship. When the shape parameters are less than two (i.e., $1 < \alpha < 2$, $1 < \beta < 2$), the gradient of the potential demonstrates a concave softening shape, which represents a plateau-type function. If the shape parameter indices are chosen as larger values (i.e., $\alpha > 2$, $\beta > 2$), the cohesive traction-separation relationship has a convex shape, which can be utilized for the analysis of quasi-brittle materials.

The PPR potential and its gradients are plotted in Fig. 12 with different fracture energies (e.g., $\phi_n = 100$ N/m, $\phi_t = 200$ N/m), cohesive strengths (e.g., $\sigma_{\max} = 40$ MPa, $\tau_{\max} = 30$ MPa), shape (e.g., $\alpha = 5$, $\beta = 1.3$) and initial slope indicators (e.g., $\lambda_n = 0.1$, $\lambda_t = 0.2$). The normal cohesive traction illustrates fracture behavior of a typical quasi-brittle material, while the tangential cohesive traction describes a plateau-type behavior. The potential-based model is also applicable when the mode I fracture energy is greater than the mode II fracture energy because the potential is explicitly derived by using the actual boundary conditions for mode I and mode II. The PPR potential-based model is utilized to investigate matrix/particle debonding [59], dynamic crack propagation, microbranching instability, and fragmentation [107,166]. Computational implementation of the model within a standard finite element method framework is straightforward if one employs an intrinsic cohesive zone modeling approach [167].

7.1 Characteristic Lengths and Cohesive Interaction Region. Since the PPR potential is based on polynomial functions, the normal and tangential traction-separation relationships are defined within a finite domain. The cohesive interaction region is determined on the basis of characteristic lengths, i.e., the final crack opening widths (δ_n, δ_t) and the conjugate final crack opening widths ($\bar{\delta}_n$, $\bar{\delta}_t$). The final crack opening widths (δ_n, δ_t) are obtained from Eq. (54), while the normal and tangential conjugate final crack opening widths ($\bar{\delta}_n$, $\bar{\delta}_t$) are evaluated by solving the following nonlinear functions:

$$f_n(\Delta_n) = \Gamma_n \left(1 - \frac{\Delta_n}{\delta_n} \right)^\alpha \left(\frac{m}{\alpha} + \frac{\Delta_n}{\delta_n} \right)^m + \langle \phi_n - \phi_t \rangle = 0 \quad (58)$$

and

$$f_t(\Delta_t) = \Gamma_t \left(1 - \frac{|\Delta_t|}{\delta_t} \right)^\beta \left(\frac{n}{\beta} + \frac{|\Delta_t|}{\delta_t} \right)^n + \langle \phi_t - \phi_n \rangle = 0 \quad (59)$$

respectively.

The normal cohesive interaction region is associated with δ_n and $\bar{\delta}_t$, while the tangential cohesive interaction region is associated with δ_t and $\bar{\delta}_n$, as illustrated in Fig. 13. When separations are within the normal cohesive interaction region (i.e., $0 \le \Delta_n \le \delta_n$ and $|\Delta_t| \le \bar{\delta}_t$), the normal cohesive traction is obtained from the PPR potential. When separations are outside of the normal interaction region, the normal cohesive traction is set to zero. Similarly, if separations are within the tangential cohesive interaction region (i.e., $0 \le \Delta_n \le \bar{\delta}_n$ and $|\Delta_t| \le \delta_t$), the tangential cohesive traction is obtained from the PPR potential. Otherwise, the tangential traction is set to zero.
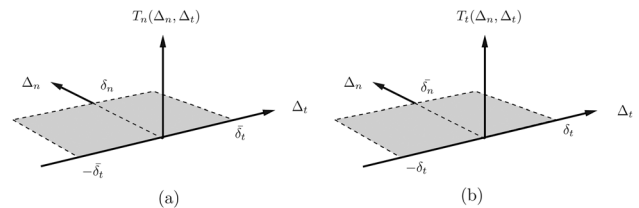

(a)　　　　　　　　　　　(b)

Fig. 13 Description of each cohesive interaction (T_n, T_t) region defined by the final crack opening widths (δ_n, δ_t) and the conjugate final crack opening widths ($\bar{\delta}_n$, $\bar{\delta}_t$); (a) T_n versus (δ_n, $\bar{\delta}_t$) space; (b) T_t versus ($\bar{\delta}_n$, δ_t) space

7.2 Extrinsic Cohesive Zone Model. The PPR potential function naturally extends to the case of the extrinsic cohesive zone model, which excludes the elastic behavior (or initial ascending part) in the cohesive interactions. The limit of the initial slope indicators in the PPR potential ($\lambda_n \to 0$ and $\lambda_t \to 0$) of Eq. (50) eliminates the initial slope indicators (λ_n, λ_t) and the exponents (m, n) from the resulting expression. Thus, the potential function for the extrinsic cohesive zone model is expressed as

$$\Psi(\Delta_n, \Delta_t) = \min(\phi_n, \phi_t) + \left[\Gamma_n \left(1 - \frac{\Delta_n}{\delta_n} \right)^\alpha + \langle \phi_n - \phi_t \rangle \right]$$
$$\times \left[\Gamma_t \left(1 - \frac{|\Delta_t|}{\delta_t} \right)^\beta + \langle \phi_t - \phi_n \rangle \right] \quad (60)$$

The gradient of the potential leads to the normal and tangential tractions along the fracture surface,

$$T_n(\Delta_n, \Delta_t) = -\alpha \frac{\Gamma_n}{\delta_n} \left(1 - \frac{\Delta_n}{\delta_n} \right)^{\alpha-1} \left[\Gamma_t \left(1 - \frac{|\Delta_t|}{\delta_t} \right)^\beta + \langle \phi_t - \phi_n \rangle \right]$$
$$T_t(\Delta_n, \Delta_t) = -\beta \frac{\Gamma_t}{\delta_t} \left(1 - \frac{|\Delta_t|}{\delta_t} \right)^{\beta-1} \left[\Gamma_n \left(1 - \frac{\Delta_n}{\delta_n} \right)^\alpha + \langle \phi_n - \phi_t \rangle \right] \frac{\Delta_t}{|\Delta_t|}$$
$$(61)$$

The tangential traction provides a finite value at the initiation point ($\Delta_t = 0$), and therefore introduces the expected discontinuity, i.e.,

$$\lim_{\Delta_t \to 0^+} T_t(\Delta_n, \Delta_t) = -\beta \frac{\Gamma_t}{\delta_t} \left[\Gamma_n \left(1 - \frac{\Delta_n}{\delta_n} \right)^\alpha + \langle \phi_n - \phi_t \rangle \right]$$
$$\lim_{\Delta_t \to 0^-} T_t(\Delta_n, \Delta_t) = \beta \frac{\Gamma_t}{\delta_t} \left[\Gamma_n \left(1 - \frac{\Delta_n}{\delta_n} \right)^\alpha + \langle \phi_n - \phi_t \rangle \right] \quad (62)$$

which is a feature of the extrinsic cohesive zone model.

The normal and tangential tractions are defined in a cohesive interaction region associated with the final crack opening width (δ_n, δ_t) and the conjugate final crack opening width ($\bar{\delta}_n$, $\bar{\delta}_t$). The final crack opening widths are expressed as

$$\delta_n = \alpha \phi_n / \sigma_{\max}, \quad \delta_t = \beta \phi_t / \tau_{\max} \quad (63)$$

which are associated with the fracture boundary conditions of $T_n(\delta_n, \Delta_t) = 0$ and $T_t(\Delta_n, \delta_t) = 0$, respectively. The conjugate final crack opening widths ($\bar{\delta}_n$, $\bar{\delta}_t$) are given in closed form

$$\bar{\delta}_n = \delta_n - \delta_n \left(\frac{\langle \phi_n - \phi_t \rangle}{\phi_n} \right)^{1/\alpha}, \bar{\delta}_t = \delta_t - \delta_t \left(\frac{\langle \phi_t - \phi_n \rangle}{\phi_t} \right)^{1/\beta} \quad (64)$$

which satisfy the conditions of $T_t(\bar{\delta}_n, \Delta_t) = 0$ and $T_n(\Delta_n, \bar{\delta}_t) = 0$, respectively. The energy constants are expressed as

$$\Gamma_n = (-\phi_n)^{\frac{\langle \phi_n - \phi_t \rangle}{\phi_n - \phi_t}}, \quad \Gamma_t = (-\phi_t)^{\frac{\langle \phi_t - \phi_n \rangle}{\phi_t - \phi_n}} \quad (\phi_n \neq \phi_t) \quad (65)$$

for the different fracture energies. If the fracture energies are the same, one obtains the energy constants,

$$\Gamma_n = -\phi_n, \quad \Gamma_t = 1 \quad (\phi_n = \phi_t) \quad (66)$$

Using the same fracture parameters, as illustrated in Fig. 12, the potential for the extrinsic cohesive zone model is plotted in Fig. 14. The initial slope is excluded, and the traction discontinuity is introduced at zero separation. In summary, rather than providing infinite slope, the cohesive interactions for the extrinsic cohesive zone model are derived by taking the limit of the initial slope indicators from the potential function. Thus, the discontinuities are naturally introduced at crack initiation.

7.3 Two- and Three-Dimensional Formulations. The PPR model is applicable for both two- and three-dimensional problems. In two-dimensional problems, the normal separation (Δ_n) corresponds to the surface normal local coordinate (Δ_1), i.e., $\Delta_n = \Delta_1$, while the tangential separation (Δ_t) agrees with the surface tangential local coordinate (Δ_2), i.e., $\Delta_t = \Delta_2$, shown in Fig. 3(a). Thus, the cohesive traction vector and the material tangent matrix (**D**) are obtained from the potential, which are expressed as

$$\mathbf{T}(\Delta_n, \Delta_t) = \begin{Bmatrix} T_1 \\ T_2 \end{Bmatrix} = \begin{Bmatrix} T_n \\ T_t \end{Bmatrix} = \begin{Bmatrix} \partial \Psi / \partial \Delta_n \\ \partial \Psi / \partial \Delta_t \end{Bmatrix} \quad (67)$$

and

$$\mathbf{D}(\Delta_n, \Delta_t) = \begin{bmatrix} D_{nn} & D_{nt} \\ D_{tn} & D_{tt} \end{bmatrix} = \begin{bmatrix} \partial^2 \Psi / \partial \Delta_n^2 & \partial^2 \Psi / \partial \Delta_n \partial \Delta_t \\ \partial^2 \Psi / \partial \Delta_t \partial \Delta_n & \partial^2 \Psi / \partial \Delta_t^2 \end{bmatrix} \quad (68)$$

when separations are within the cohesive interaction region.

In three-dimensional problems, the out-of-plane separation (Δ_1) matches the normal separation (Δ_n). The in-plane separations (Δ_2, Δ_3) are related to the tangential separation (Δ_t) by introducing an effective quantity [168], i.e., $\Delta_t = \sqrt{\Delta_2^2 + \Delta_3^2}$ (Fig. 3(b)). The substitution of the effective quantity into the PPR potential expression and the gradient of the potential lead to a cohesive traction vector

$$\mathbf{T} = \begin{Bmatrix} \partial \Psi / \partial \Delta_1 \\ \partial \Psi / \partial \Delta_2 \\ \partial \Psi / \partial \Delta_3 \end{Bmatrix} = \begin{Bmatrix} T_1 \\ T_2 \\ T_3 \end{Bmatrix} = \begin{Bmatrix} T_n \\ T_t \Delta_2 / \Delta_t \\ T_t \Delta_3 / \Delta_t \end{Bmatrix} \quad (69)$$

where T_1, T_2, and T_3 are cohesive tractions along the separation directions of Δ_1, Δ_2, and Δ_3, respectively. The second derivatives of the PPR potential with respect to the separations in the local coordinates result in the material tangent matrix,

$$\mathbf{D} = \begin{bmatrix} D_{nn} & D_{nt}\Delta_2/\Delta_t & D_{nt}\Delta_3/\Delta_t \\ D_{tn}\Delta_2/\Delta_t & D_{tt}\Delta_2^2/\Delta_t^2 + T_t\Delta_3^2/\Delta_t^3 & D_{tt}\Delta_2\Delta_3/\Delta_t^2 - T_t\Delta_2\Delta_3/\Delta_t^3 \\ D_{tn}\Delta_3/\Delta_t & D_{tt}\Delta_2\Delta_3/\Delta_t^2 - T_t\Delta_2\Delta_3/\Delta_t^3 & D_{tt}\Delta_3^2/\Delta_t^2 + T_t\Delta_2^2/\Delta_t^3 \end{bmatrix} \quad (70)$$

7.4 Path Dependence of Work-of-Separation. The PPR model provides a consistent constitutive relationship under mixed-mode conditions. The consistency of the traction-separation relationship is demonstrated by assessing the work-of-separation [3,161]. The work-of-separation (W_{sep}) consists of the work done (W_n) by the normal traction and the work done (W_t) by
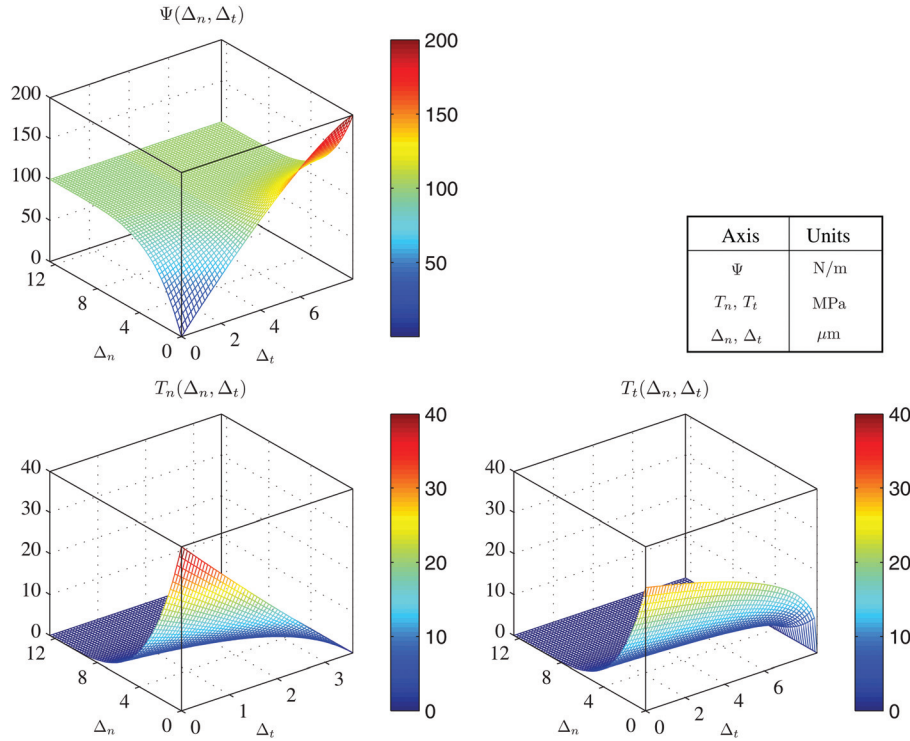
Fig. 14 The PPR potential [3] and its gradients for the extrinsic cohesive zone model with $\phi_n = 100$ N/m, $\phi_t = 200$ N/m, $\sigma_{max} = 40$ MPa, $\tau_{max} = 30$ MPa, $\alpha = 5$, and $\beta = 1.3$

the tangential traction. Two separation paths are investigated. First, material particles separate along the normal direction up to $\Delta_n = \Delta_{n,max}$, and then the complete tangential failure occurs, i.e., Path 1 in Fig. 15(a). In this case, the work-of-separation is evaluated by the following expression:

$$W_{sep} = \underbrace{\int_0^{\Delta_{n,max}} T_n(\Delta_n, 0) d\Delta_n}_{W_n} + \underbrace{\int_0^{\delta_t} T_t(\Delta_{n,max}, \Delta_t) d\Delta_t}_{W_t} \quad (71)$$

For the other path, material particles separate along the tangential direction up to $\Delta_t = \Delta_{t,max}$, and then the complete normal failure occurs, i.e., **Path 2** in Fig. 15(b). Accordingly, the work-of-separation for the second path is expressed as

$$W_{sep} = \underbrace{\int_0^{\Delta_{t,max}} T_t(0, \Delta_t) d\Delta_t}_{W_t} + \underbrace{\int_0^{\delta_n} T_n(\Delta_n, \Delta_{t,max}) d\Delta_n}_{W_n} \quad (72)$$

Fracture parameters in the PPR model are arbitrarily selected as $\phi_n = 100$ N/m, $\phi_t = 200$ N/m, $\sigma_{max} = 3$ MPa, $\tau_{max} = 12$ MPa,

$\alpha = 3$, $\beta = 3$, $\lambda_n = 0.01$ and $\lambda_t = 0.01$. The variation of the work-of-separation is illustrated in Fig. 16. For **Path 1**, $\Delta_{n,max} = 0$ indicates the mode II failure while $\Delta_{n,max} = \delta_n$ represents the mode I failure. Thus, while $\Delta_{n,max}$ increases from zero to δ_n, the work-of-separation (W_{sep}) monotonically decreases from the mode II fracture energy (ϕ_t) to the mode I fracture energy (ϕ_n). The work done (W_n) by the normal traction increases from 0 to ϕ_n while the work done (W_t) by the tangential traction decreases from ϕ_t to zero.

For **Path 2**, the separation path corresponds to the mode I failure when $\Delta_{t,max} = 0$ and to the mode II failure when $\Delta_{t,max} = \delta_t$. The increase of $\Delta_{t,max}$ from 0 to δ_t leads to the monotonic increase of W_{sep} from ϕ_n to ϕ_t although there is a kink point, as illustrated in Fig. 16(b). The separation at the kink point corresponds to the tangential conjugate final crack opening width ($\bar{\delta}_t$). When the tangential separation is smaller than $\bar{\delta}_t$, the normal cohesive traction is obtained from the potential function. When $\Delta_t > \bar{\delta}_t$, the normal cohesive traction is zero. Thus, the normal cohesive traction is not smooth but piece-wise continuous at $\Delta_t = \bar{\delta}_t$ in this example. The work-of-separation (W_{sep}) and the work done (W_n) by the normal cohesive traction are associated with the integration of the normal cohesive traction, and therefore, W_{sep} and W_n are also piece-wise continuous.
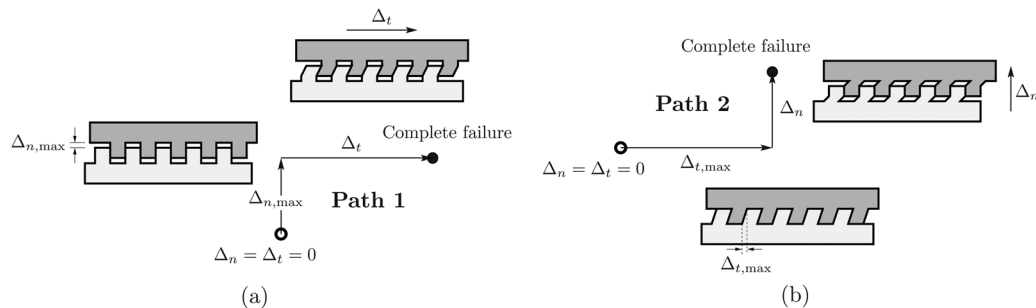

Fig. 15 Two arbitrary separation paths for the material debonding process; (a) nonproportional path 1; (b) nonproportional path 2
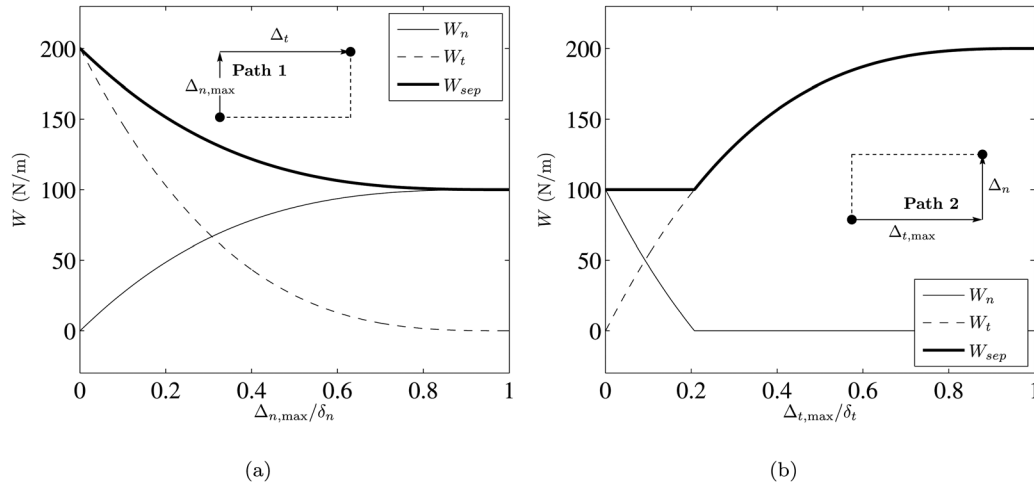
Fig. 16 Variation of the work-of-separation considering the PPR potential [3] ($\phi_n = 100\,\text{N/m}$, $\phi_t = 200\,\text{N/m}$); (*a*) nonproportional path 1; (*b*) nonproportional path 2

8 Concluding Remarks

This review article provides a critique of constitutive relationships for cohesive zone models, with an emphasis on potential-based models. Several effective displacement-based models [98,135,136,138,139] are formulated in a single framework by modifying the effective traction ($\bar{T}$) and a mode-mixity parameter (α_e). The model provides various shapes of the effective traction-separation ($\bar{T} - \bar{\Delta}$) relation. However, the model can provide positive stiffness under softening conditions, and thus the increase of separation results in the increase of the corresponding traction. General potential-based models are expressed in terms of normal and tangential separations (Δ_n, Δ_t) rather than an effective quantity. The general potential-based models with polynomials [4,5] are based on cubic-polynomials for the normal cohesive traction in conjunction with a linear tangential traction. Because of the linear tangential traction, the mode II fracture energy is unbounded, and thus these models should either not be utilized or be utilized with caution for problems that have significant tangential separation. The general potential-based models with the universal binding energy [7–9] are chronologically reviewed. The exponential-periodic potential-based model [7] was generalized by applying several boundary conditions associated with cohesive fracture [8]. In order to account for complete shear failure in the generalized exponential-periodic potential-based model [8], the exponential-exponential potential-based model was proposed [9]. However, the exponential-exponential potential-based model has issues on boundary conditions associated with the complete failure condition, especially when the mode I fracture energy is different from the mode II fracture energy. Additionally, the models with exponential expressions are based on an atomistic potential which includes elastic behavior, and thus the traction-separation relationships can lead to a significant artificial elastic range that is not controllable. Alternatively, the unified potential-based model [3] is derived on the basis of consistent boundary conditions associated with fracture parameters such as fracture energy, cohesive strength, shape and initial slope. However, potential-based models still possess several limitations on representing physical phenomena associated with cohesive fracture, as discussed below:

- The presented potential-based models are proposed under the condition of monotonic separation paths. Thus, unloading/reloading relations should be addressed independently in order to describe energy dissipations, which include fatigue damage.
- The reviewed potential functions are rate independent. In order to account for rate-dependent fracture behaviors, the potential-based models may need additional constraints or a rate-dependent potential-based model may need to be developed.

- Potential-based models of cohesive fracture mostly focus on a softening condition. When compression acts on the fracture surface, a penalty stiffness is generally introduced, and thus the models provide negative normal separations. In order to accurately represent contact, friction, and its rate dependence along the fracture surface under compression, one may need to introduce additional constitutive relationships.
- The unified potential-based model is determined on the basis of four fracture parameters in each fracture mode. The determination of the fracture parameters are a challenging task, especially for the shearing mode.

In conclusion, the constitutive relationship of mixed-mode cohesive fracture should be selected with great caution.

Nomenclature

$\langle \cdot \rangle$ = Macaulay bracket
Γ_n, Γ_t = energy constants in the PPR model
$\underline{\Delta}$ = nondimensional effective displacement
$\bar{\Delta}$ = effective displacement
Δ_n, Δ_t = normal and tangential separations
$\Delta_{n,\max}, \Delta_{t,\max}$ = maximum normal and tangential separations in a separation path
Δ_n^* = length scale parameter in the exponential potential-based model
Δ_t = in-plane tangential separation vector
$\Delta_1, \Delta_2, \Delta_3$ = separations along the local coordinate system
Ψ = potential for cohesive fracture
α, β = shape parameters in the PPR model
α_e, β_e = nondimensional constant in the effective displacement-based model
β_s = nondimensional constant in the exponential potential-based model
α_s = shear stiffness parameter
α_2, α_3 = nondimensional constant associated with mode-mixity in three-dimensions

γ_s = surface energy
γ_{us} = unstable stacking energy
δ_n, δ_t = normal and tangential characteristic lengths
δ_{nc}, δ_{tc} = critical normal and tangential crack opening widths in the PPR model
$\bar{\delta}_n, \bar{\delta}_t$ = normal and tangential conjugate final crack opening widths in the PPR model
$\delta_1, \delta_2, \delta_3$ = characteristic lengths in three-dimensions
δ_c^* = internal length scale variable
λ_n, λ_t = initial slope indicators
θ = phase angle
$\sigma_{\max}, \tau_{\max}$ = cohesive strength
ϕ_n, ϕ_t = fracture energy
$\mathbf{D}$ = tangent matrix
$D_{\min}$ = internal parameter
D_s = internal residual strength variable
E_0 = initial modulus of an interface layer
$\mathbf{T}$ = cohesive traction vector
$\bar{T}, \widetilde{T}$ = effective traction
T_n, T_t = normal and tangential cohesive tractions
T_1, T_2, T_3 = cohesive tractions along the local coordinate system
W_{sep} = work-of-separation
W_n, W_t = work done by normal and tangential traction
ℓ = scaled separation associated with the Thomas–Fermi screening length
m, n = nondimensional exponents in the PPR model
$\mathbf{n}_n$ = unit normal separation vector with respect to the cohesive surface
$\mathbf{n}_t$ = unit in-plane tangential separation vector with respect to the cohesive surface
q = ratio of the mode II fracture energy to the mode I fracture energy
r = nondimensional parameter associated with length scales
t_0^* = internal cohesive traction variable
z = nondimensional constant in the exponential potential-based model

References

[1] Gurtin, M. E., 1981, *An Introduction to Continuum Mechanics*, Academic Press, New York.
[2] Needleman, A., 1992, "Micromechanical Modelling of Interfacial Decohesion," Ultramicroscopy, **40**(3), pp. 203–214.
[3] Park, K., Paulino, G. H., and Roesler, J. R., 2009, "A Unified Potential-Based Cohesive Model of Mixed-Mode Fracture," J. Mech. Phys. Solids, **57**(6), pp. 891–908.
[4] Needleman, A., 1987, "A Continuum Model for Void Nucleation by Inclusion Debonding," ASME J. Appl. Mech., **54**(3), pp. 525–531.
[5] Freed, Y., and Banks-Sills, L., 2008, "A New Cohesive Zone Model for Mixed Mode Interface Fracture in Bimaterials," Eng. Fract. Mech., **75**(15), pp. 4583–4593.
[6] Needleman, A., 1990, "An Analysis of Decohesion Along an Imperfect Interface," Int. J. Fract., **42**(1), pp. 21–40.
[7] Needleman, A., 1990, "An Analysis of Tensile Decohesion Along an Interface," J. Mech. Phys. Solids, **38**(3), pp. 289–324.
[8] Beltz, G. E., and Rice, J. R., 1991, "Dislocation Nucleation Versus Cleavage Decohesion at Crack Tips," *Modeling the Deformation of Crystalline Solids Presented*, T. C. Lowe, A. D. Rollett, P. S. Follansbee, and G. S. Daehn, eds., The Minerals, Metals & Materials Society, Harvard University, Cambridge, MA, pp. 457–480.
[9] Xu, X. P., and Needleman, A., 1993, "Void Nucleation by Inclusion Debonding in a Crystal Matrix," Model. Simul. Mater. Sci. Eng., **1**(2), pp. 111–132.
[10] Kanninen, M. F., and Popelar, C. H., 1985, *Advanced Fracture Mechanics*, Oxford University Press, New York.
[11] Bazant, Z. P., and Cedolin, L., 1991, *Stability of Structures: Elastic, Inelastic, Fracture, and Damage Theories*, Oxford University Press, New York.
[12] Anderson, T. L., 1995, *Fracture Mechanics: Fundamentals and Applications*, CRC Press, Boca Raton, FL.
[13] Suresh, S., 1998, *Fatigue of Materials*, Cambridge University Press, New York.
[14] Broberg, K. B., 1999, *Cracks and Fracture*, Academic Press, San Diego, CA.
[15] Elliott, H. A., 1947, "An Analysis of the Conditions for Rupture Due to Griffith Cracks," Proc. Phys. Soc., **59**(2), pp. 208–223.
[16] Barenblatt, G. I., 1959, "The Formation of Equilibrium Cracks During Brittle Fracture: General Ideas and Hypotheses, Axially Symmetric Cracks," Appl. Math. Mech., **23**(3), pp. 622–636.
[17] Barenblatt, G. I., 1962, "The Mathematical Theory of Equilibrium Cracks in Brittle Fracture," Adv. Appl. Mech., **7**, pp. 55–129.
[18] Dugdale, D. S., 1960, "Yielding of Steel Sheets Containing Slits," J. Mech. Phys. Solids, **8**(2), pp. 100–104.
[19] Griffith, A. A., 1921, "The Phenomena of Rupture and Flow in Solids," Philos. Trans. R. Soc. London, **221**, pp. 163–198.
[20] Willis, J. R., 1967, "A Comparison of the Fracture Criteria of Griffith and Barenblatt," J. Mech. Phys. Solids, **15**(3), pp. 151–162.
[21] Rice, J. R., 1968, "A Path Independent Integral and the Approximate Analysis of Strain Concentration by Notches and Cracks," ASME J. Appl. Mech., **35**(2), pp. 379–386.
[22] Bilby, B. A., Cottrell, A. H., and Swinden, K. H., 1963, "Spread of Plastic Yield From Notch," R. Soc. Proc. Ser. A, **272**(1350), pp. 304–314.
[23] Bilby, B. A., and Swinden, K. H., 1965, "Representation of Plasticity at Notches by Linear Dislocations Arrays," R. Soc. Proc. Ser. A, **285**(1400), pp. 22–33.
[24] Rice, J. R., 1968, "Mathematical Analysis in the Mechanics of Fracture," *Fracture: An Advanced Treatise*, Vol. 2, H. Liebowitz, ed., Academic Press, New York, pp. 191–311.
[25] Smith, E., 1974, "The Structure in the Vicinity of a Crack Tip: A General Theory Based on the Cohesive Zone Model," Eng. Fract. Mech., **6**(2), pp. 213–222.
[26] Keer, L. M., 1964, "Stress Distribution at the Edge of an Equilibrium Crack," J. Mech. Phys. Solids, **12**(3), pp. 149–163.
[27] Cribb, J. L., and Tomkins, B., 1967, "On the Nature of the Stress at the Tip of a Perfectly Brittle Crack," J. Mech. Phys. Solids, **15**(2), pp. 135–140.
[28] Smith, E., 1975, "A Generalization of Elliott's Model of a Crack Tip," Int. J. Fract., **11**(2), pp. 295–299.
[29] Hillerborg, A., Modeer, M., and Petersson, P. E., 1976, "Analysis of Crack Formation and Crack Growth in Concrete by Means of Fracture Mechanics and Finite Elements," Cem. Concr. Res., **6**(6), pp. 773–781.
[30] Boone, T. J., Wawrzynek, P. A., and Ingraffea, A. R., 1986, "Simulation of the Fracture Process in Rock With Application to Hydrofracturing," Int. J. Rock Mech. Min. Sci., **23**(3), pp. 255–265.
[31] Elices, M., Guinea, G. V., Gomez, J., and Planas, J., 2002, "The Cohesive Zone Model: Advantages, Limitations and Challenges," Eng. Fract. Mech., **69**(2), pp. 137–163.
[32] Bazant, Z. P., and Becq-Giraudon, E., 2002, "Statistical Prediction of Fracture Parameters of Concrete and Implications for Choice of Testing Standard," Cem. Concr. Res., **32**(4), pp. 529–556.
[33] Roesler, J., Paulino, G. H., Park, K., and Gaedicke, C., 2007, "Concrete Fracture Prediction Using Bilinear Softening," Cem. Concr. Compos., **29**(4), pp. 300–312.
[34] Petersson, P. E., 1981, "Crack Growth and Development of Fracture Zones in Plain Concrete and Similar Materials," Tech. Report No. LUTVDG/TVBM-1006, Lund Institute of Technology, Sweden.
[35] Wittmann, F. H., Rokugo, K., Bruehwiler, E., Mihashi, H., and Simonin, P., 1988, "Fracture Energy and Strain Softening of Concrete as Determined by Means of Compact Tension Specimens," Mater. Struct., **21**(1), pp. 21–32.
[36] Guinea, G. V., Planas, J., and Elices, M., 1994, "A General Bilinear Fit for the Softening Curve of Concrete," Materiaux Constr., **27**(2), pp. 99–105.
[37] Park, K., Paulino, G. H., and Roesler, J. R., 2008, "Determination of the Kink Point in the Bilinear Softening Model for Concrete," Eng. Fract. Mech., **75**(13), pp. 3806–3818.
[38] Jenq, Y. S., and Shah, S. P., 1985, "Two Parameter Fracture Model for Concrete," JSCE J. –Eng. Mech., **111**(10), pp. 1227–1241.
[39] Bazant, Z. P., and Kazemi, M. T., 1990, "Determination of Fracture Energy, Process Zone Length and Brittleness Number From Size Effect, With Application to Rock and Concrete," Int. J. Fract., **44**(2), pp. 111–131.
[40] Shah, S. P., Swartz, S. E., and Ouyang, C., 1995, *Fracture Mechanics of Concrete: Applications of Fracture Mechanics to Concrete, Rock and Other Quasi-Brittle Materials*, Wiley-Interscience, New York.
[41] van Mier, J. G. M., 1996, *Fracture Processes of Concrete: Assessment of Material Parameters for Fracture Models*, CRC Press, Boca Raton, FL.
[42] Bazant, Z. P., and Planas, J., 1998, *Fracture and Size Effect in Concrete and other Quasibrittle Materials*, CRC Press, Boca Raton, FL.
[43] Li, V. C., Stang, H., and Krenchel, H., 1993, "Micromechanics of Crack Bridging in Fibre-Reinforced Concrete," Mater. Struct., **26**(162), pp. 486–494.
[44] Park, K., Paulino, G. H., and Roesler, J., 2010, "Cohesive Fracture Model for Functionally Graded Fiber Reinforced Concrete," Cem. Concr. Res., **40**(6), pp. 956–965.
[45] Hui, C. Y., Ruina, A., Long, R., and Jagota, A., 2011, "Cohesive Zone Models and Fracture," J. Adhes., **87**(1), pp. 1–52.
[46] Kramer, E. J., 1983, "Microscopic and Molecular Fundamentals of Crazing," *Crazing in Polymers* (Advances in Polymer Science), Vol. 52–53, H. Kausch, ed., Springer-Verlag, Berlin, Germany, pp. 1–56.
[47] Tijssens, M. G. A., van der Giessen, E., and Sluys, L. J., 2000, "Modeling of Crazing Using a Cohesive Surface Methodology," Mech. Mater., **32**(1), pp. 19–35.
[48] Estevez, R., Tijssens, M. G. A., and der Giessen, E. V., 2000, "Modeling of the Competition Between Shear Yielding and Crazing in Glassy Polymers," J. Mech. Phys. Solids, **48**(12), pp. 2585–2617.
[49] Allen, D. H., and Searcy, C. R., 2001, "Micromechanical Model for a Viscoelastic Cohesive Zone," Int. J. Fract., **107**(2), pp. 159–176.

[50] Hui, C. Y., Ruina, A., Creton, C., and Kramer, E. J., 1992, "Micromechanics of Crack Growth Into a Craze in a Polymer Glass," Macromolecules, 25(15), pp. 3948–3955.

[51] Hui, C. Y., and Kramer, E. J., 1995, "Molecular Weight Dependence of the Fracture Toughness of Glassy Polymers Arising From Crack Propagation Through a Craze," Polym. Eng. Sci., 35(5), pp. 419–425.

[52] Hong, S., Chew, H. B., and Kim, K.-S., 2009, "Cohesive-Zone Laws for Void Growth – I. Experimental Field Projection of Crack-Tip Crazing in Glassy Polymers," J. Mech. Phys. Solids, 57(8), pp. 1357–1373.

[53] Bolander, J. E., and Sukumar, N., 2005, "Irregular Lattice Model for Quasi-static Crack Propagation," Phys. Rev. B, 71(9), p. 094106.

[54] Li, S., and Ghosh, S., 2006, "Extended Voronoi Cell Finite Element Model for Multiple Cohesive Crack Propagation in Brittle Materials," Int. J. Numer. Methods Eng., 65(7), pp. 1028–1067.

[55] Bishop, J. E., 2009, "Simulating the Pervasive Fracture of Materials and Structures Using Randomly Close Packed Voronoi Tessellations," Comput. Mech., 44(4), pp. 455–471.

[56] Walter, M. E., Ravichandran, G., and Ortiz, M., 1997, "Computational Modeling of Damage Evolution in Unidirectional Fiber Reinforced Ceramic Matrix Composites," Comput. Mech., 20(1–2), pp. 192–198.

[57] Carpinteri, A., Paggi, M., and Zavarise, G., 2005, "Snap-Back Instability in Micro-Structured Composites and its Connection With Superplasticity," Strength, Fract. Complexity, 3(2–4), pp. 61–72.

[58] Needleman, A., Borders, T. L., Brinson, L. C., Flores, V. M., and Schadler, L. S., 2010, "Effect of an Interphase Region on Debonding of a CNT Reinforced Polymer Composite," Compos. Sci. Technol., 70(15), pp. 2207–2215.

[59] Ngo, D., Park, K., Paulino, G. H., and Huang, Y., 2010, "On the Constitutive Relation of Materials With Microstructure Using a Potential-Based Cohesive Model for Interface Interaction," Eng. Fract. Mech., 77(7), pp. 1153–1174.

[60] Paulino, G. H., Jin, Z. H., and Dodds, R. H., 2003, "Failure of Functionally Graded Materials," Comprehensive Structural Integrity, Vol. 2, B. Karihaloo and W. G. Knauss, eds., Elsevier, The Netherlands, pp. 607–644.

[61] Erdogan, F., and Sih, G. C., 1963, "On the Crack Extension in Plates Under Plane Loading and Transverse Shear," ASME J. Basic Eng., 85(4), pp. 519–525.

[62] Pindera, M.-J., and Paulino, G. H., 2008, "Honoring Professor Erdogan's Seminal Contributions to Mixed Boundary-Value Problems of Inhomogeneous and Functionally Graded Materials," ASME J. Appl. Mech., 75(5), p. 050301.

[63] Erdogan, F., and Ozturk, M., 2008, "On the Singularities in Fracture and Contact Mechanics," ASME J. Appl. Mech., 75(5), p. 051111.

[64] Dag, S., and Ilhan, K. A., 2008, "Mixed-Mode Fracture Analysis of Orthotropic Functionally Graded Material Coatings Using Analytical and Computational Methods," ASME J. Appl. Mech., 75(5), p. 051104.

[65] Tvergaard, V., 2002, "Theoretical Investigation of the Effect of Plasticity on Crack Growth Along a Functionally Graded Region Between Dissimilar Elastic-Plastic Solids," Eng. Fract. Mech., 69(14–16), pp. 1635–1645.

[66] Wang, Z., and Nakamura, T., 2004, "Simulations of Crack Propagation in Elastic-Plastic Graded Materials," Mech. Mater., 36(7), pp. 601–622.

[67] Jin, Z.-H., Paulino, G. H., and Dodds, R. H., Jr., 2003, "Cohesive Fracture Modeling of Elastic-Plastic Crack Growth in Functionally Graded Materials," Eng. Fract. Mech., 70(14), pp. 1885–1912.

[68] Rangaraj, S., and Kokini, K., 2004, "A Study of Thermal Fracture in Functionally Graded Thermal Barrier Coatings Using a Cohesive Zone Model," ASME J. Eng. Mater. Technol., 126(1), pp. 103–115.

[69] Zhang, Z., and Paulino, G. H., 2005, "Cohesive Zone Modeling of Dynamic Failure in Homogeneous and Functionally Graded Materials," Int. J. Plast., 21(6), pp. 1195–1254.

[70] Kandula, S. S. V., Abanto-Bueno, J., Geubelle, P. H., and Lambros, J., 2005, "Cohesive Modeling of Dynamic Fracture in Functionally Graded Materials," Int. J. Fract., 132(3), pp. 275–296.

[71] Jin, Z.-H., Paulino, G. H., and Dodds, R. H., 2002, "Finite Element Investigation of Quasi-Static Crack Growth in Functionally Graded Materials Using a Novel Cohesive Zone Fracture Model," ASME J. Appl. Mech., 69(3), pp. 370–379.

[72] Shim, D.-J., Paulino, G. H., and Dodds, R. H., Jr., 2006, "J Resistance Behavior in Functionally Graded Materials Using Cohesive Zone and Modified Boundary Layer Models," Int. J. Fract., 139(1), pp. 91–117.

[73] Brocks, W., and Cornec, A., 2003, "Guest Editorial: Cohesive Models," Eng. Fract. Mech., 70(14), pp. 1741–1742.

[74] de Andres, A., Perez, J. L., and Ortiz, M., 1999, "Elastoplastic Finite Element Analysis of Three Dimensional Fatigue Crack Growth in Aluminum Shafts Subjected to Axial Loading," Int. J. Solids Struct., 36(15), pp. 2231–2258.

[75] Deshpande, V. S., Needleman, A., and Van der Giessen, E., 2001, "A Discrete Dislocation Analysis of Near-Threshold Fatigue Crack Growth," Acta Mater., 49(16), pp. 3189–3203.

[76] Roe, K. L., and Siegmund, T., 2003, "An Irreversible Cohesive Zone Model for Interface Fatigue Crack Growth Simulation," Eng. Fract. Mech., 70(2), pp. 209–232.

[77] Maiti, S., and Geubelle, P. H., 2005, "A Cohesive Model for Fatigue Failure of Polymers," Eng. Fract. Mech., 72(5), pp. 691–708.

[78] Ural, A., Krishnan, V. R., and Papoulia, K. D., 2009, "A Cohesive Zone Model for Fatigue Crack Growth Allowing for Crack Retardation," Int. J. Solids Struct., 46(11–12), pp. 2453–2462.

[79] Ingraffea, A. R., Gerstle, W. H., Gergely, P., and Saouma, V., 1984, "Fracture Mechanics of Bond in Reinforced Concrete," J. Struct. Eng., 110(4), pp. 871–890.

[80] Prasad, M. V. K. V., and Krishnamoorthy, C. S., 2002, "Computational Model for Discrete Crack Growth in Plain and Reinforced Concrete," Comput. Methods Appl. Mech. Eng., 191(25–26), pp. 2699–2725.

[81] Koeberl, B., and Willam, K., 2008, "Question of Tension Softening Versus Tension Stiffening in Plain and Reinforced Concrete," ASCE J. Eng. Mech., 134(9), pp. 804–808.

[82] Yang, Q. D., and Thouless, M. D., 2001, "Mixed-Mode Fracture Analyses of Plastically-Deforming Adhesive Joints," Int. J. Fract., 110(2), pp. 175–187.

[83] Xu, C., Siegmund, T., and Ramani, K., 2003, "Rate-Dependent Crack Growth in Adhesives: I. Modeling Approach," Int. J. Adhes. Adhes., 23(1), pp. 9–13.

[84] Alfano, M., Furgiuele, F., Leonardi, A., Maletta, C., and Paulino, G. H., 2009, "Mode I Fracture of Adhesive Joints Using Tailored Cohesive Zone Models," Int. J. Fract., 157(1–2), pp. 193–204.

[85] Khoramishad, H., Crocombe, A. D., Katnam, K. B., and Ashcroft, I. A., 2010, "Predicting Fatigue Damage in Adhesively Bonded Joints Using a Cohesive Zone Model," Int. J. Fatigue, 32(7), pp. 1146–1158.

[86] Miller, O., Freund, L. B., and Needleman, A., 1999, "Energy Dissipation in Dynamic Fracture of Brittle Materials," Model. Simul. Mater. Sci. Eng., 7(4), pp. 573–586.

[87] Zhang, Z., Paulino, G. H., and Celes, W., 2007, "Extrinsic Cohesive Modeling of Dynamic Fracture and Microbranching Instability in Brittle Materials," Int. J. Numer. Methods Eng., 72(8), pp. 893–923.

[88] Rabczuk, T., Song, J.-H., and Belytschko, T., 2009, "Simulations of Instability in Dynamic Fracture by the Cracking Particles Method," Eng. Fract. Mech., 76(6), pp. 730–741.

[89] Pandolfi, A., Krysl, P., and Ortiz, M., 1999, "Finite Element Simulation of Ring Expansion and Fragmentation: The Capturing of Length and Time Scales Through Cohesive Models of Fracture," Int. J. Fract., 95(1–4), pp. 279–297.

[90] Zhou, F., Molinari, J.-F., and Ramesh, K. T., 2005, "A Cohesive Model Based Fragmentation Analysis: Effects of Strain Rate and Initial Defects Distribution," Int. J. Solids Struct., 42(18–19), pp. 5181–5207.

[91] Molinari, J. F., Gazonas, G., Raghupathy, R., Rusinek, A., and Zhou, F., 2007, "The Cohesive Element Approach to Dynamic Fragmentation: The Question of Energy Convergence," Int. J. Numer. Methods Eng., 69(3), pp. 484–503.

[92] Reeder, J. R., and Crews, J. H., Jr., 1990, "Mixed-Mode Bending Method for Delamination Testing," AIAA J., 28(7), pp. 1270–1276.

[93] Benzeggagh, M. L., and Kenane, M., 1996, "Measurement of Mixed-Mode Delamination Fracture Toughness of Unidirectional Glass/Epoxy Composites With Mixed-Mode Bending Apparatus," Compos. Sci. Technol., 56(4), pp. 439–449.

[94] Banks-Sills, L., Travitzky, N., Ashkenazi, D., and Eliasi, R., 1999, "A Methodology for Measuring Interface Fracture Properties of Composite Materials," Int. J. Fract., 99(3), pp. 143–160.

[95] Zhu, Y., Liechti, K. M., and Ravi-Chandar, K., 2009, "Direct Extraction of Rate-Dependent Traction Separation Laws for Polyurea/Steel Interfaces," Int. J. Solids Struct., 46(1), pp. 31–51.

[96] Xu, X. P., and Needleman, A., 1994, "Numerical Simulations of Fast Crack Growth in Brittle Solids," J. Mech. Phys. Solids, 42(9), pp. 1397–1434.

[97] Camacho, G. T., and Ortiz, M., 1996, "Computational Modelling of Impact Damage in Brittle Materials," Int. J. Solids Struct., 33(20–22), pp. 2899–2938.

[98] Ortiz, M., and Pandolfi, A., 1999, "Finite-Deformation Irreversible Cohesive Elements for Three Dimensional Crack-Propagation Analysis," Int. J. Numer. Methods Eng., 44(9), pp. 1267–1282.

[99] Celes, W., Paulino, G. H., and Espinha, R., 2005, "A Compact Adjacency-Based Topological Data Structure for Finite Element Mesh Representation," Int. J. Numer. Methods Eng., 64(11), pp. 1529–1556.

[100] Celes, W., Paulino, G. H., and Espinha, R., 2005, "Efficient Handling of Implicit Entities in Reduced Mesh Representations," J. Comput. Info. Sci. Eng., 5(4), pp. 348–359.

[101] Mota, A., Knap, J., and Ortiz, M., 2008, "Fracture and Fragmentation of Simplicial Finite Element Meshes Using Graphs," Int. J. Numer. Methods Eng., 73(11), pp. 1547–1570.

[102] Espinha, R., Celes, W., Rodriguez, N., and Paulino, G. H., 2009, "ParTopS: Compact Topological Framework for Parallel Fragmentation Simulations," Eng. Comput., 25(4), pp. 345–365.

[103] Wells, G. N., and Sluys, L. J., 2001, "A New Method for Modelling Cohesive Cracks Using Finite Elements," Int. J. Numer. Methods Eng., 50(12), pp. 2667–2682.

[104] Moes, N., and Belytschko, T., 2002, "Extended Finite Element Method for Cohesive Crack Growth," Eng. Fract. Mech., 69(7), pp. 813–833.

[105] Remmers, J. J. C., de Borst, R., and Needleman, A., 2008, "The Simulation of Dynamic Crack Propagation Using the Cohesive Segments Method," J. Mech. Phys. Solids, 56(1), pp. 70–92.

[106] Song, J.-H., and Belytschko, T., 2009, "Cracking Node Method for Dynamic Fracture With Finite Elements," Int. J. Numer. Methods Eng., 77(3), pp. 360–385.

[107] Paulino, G. H., Park, K., Celes, W., and Espinha, R., 2010, "Adaptive Dynamic Cohesive Fracture Simulation Using Edge-Swap and Nodal Perturbation Operators," Int. J. Numer. Methods Eng., 84(11), pp. 1303–1343.

[108] Simo, J. C., Oliver, J., and Armero, F., 1993, "An Analysis of Strong Discontinuities Induced by Strain Softening in Rate-Independent Inelastic Solids," Comput. Mech., 12(5), pp. 277–296.

[109] Oliver, J., Huespe, A. E., Pulido, M. D. G., and Chaves, E., 2002, "From Continuum Mechanics to Fracture Mechanics: The Strong Discontinuity Approach," Eng. Fract. Mech., 69(2), pp. 113–136.

[110] Linder, C., and Armero, F., 2007, "Finite Elements With Embedded Strong Discontinuities for the Modeling of Failure in Solids," Int. J. Numer. Methods Eng., 72(12), pp. 1391–1433.

[111] Carol, I., Prat, P. C., and Lopez, C. M., 1997, "Normal/Shear Cracking Model: Application to Discrete Crack Analysis," ASCE J. Eng. Mech., **123**(8), pp. 765–773.

[112] Willam, K., Rhee, I., and Shing, B., 2004, "Interface Damage Model for Thermomechanical Degradation of Heterogeneous Materials," Comput. Methods Appl. Mech. Eng., **193**(30–32), pp. 3327–3350.

[113] Caballero, A., Willam, K. J., and Carol, I., 2008, "Consistent Tangent Formulation for 3D Interface Modeling of Cracking/Fracture in Quasi-Brittle Materials," Comput. Methods Appl. Mech. Eng., **197**(33–40), pp. 2804–2822.

[114] Segura, J. M., and Carol, I., 2010, "Numerical Modelling of Pressurized Fracture Evolution in Concrete Using Zero-Thickness Interface Elements," Eng. Fract. Mech., **77**(9), pp. 1386–1399.

[115] Gao, H., and Klein, P., 1998, "Numerical Simulation of Crack Growth in an Isotropic Solid With Randomized Internal Cohesive Bonds," J. Meh. Phys. Solids, **46**(2), pp. 187–218.

[116] Gao, H., and Ji, B., 2003, "Modeling Fracture in Nanomaterials via a Virtual Internal Bond Method," Eng. Fract. Mech., **70**(14), pp. 1777–1791.

[117] Park, K., Paulino, G. H., and Roesler, J. R., 2008, "Virtual Internal Pair-Bond (VIPB) Model for Quasi-Brittle Materials," ASCE J. Eng. Mech., **134**(10), pp. 856–866.

[118] Bazant, Z. P., 1984, "Microplane Model for Strain-Controlled Inelastic Behavior," *Mechanics of Engineering Materials*, C. S. Desai and R. H. Gallagher, eds., Prentice-Hall, Englewood Cliffs, NJ, pp. 45–59.

[119] Bazant, Z. P., and Oh, B. H., 1985, "Microplane Model for Progressive Fracture of Concrete and Rock," ASCE J. Eng. Mech., **111**(4), pp. 559–582.

[120] Bazant, Z. P., and Caner, F. C., 2005, "Microplane Model M5 With Kinematic and Static Constraints for Concrete Fracture and Anelasticity I: Theory," ASCE J. Eng. Mech., **131**(1), pp. 31–40.

[121] Silling, S. A., 2000, "Reformulation of Elasticity Theory for Discontinuities and Long-Range Forces," J. Mech. Phys. Solids, **48**(1), pp. 175–209.

[122] Macek, R. W., and Silling, S. A., 2007, "Peridynamics via Finite Element Analysis," Finite Elem. Anal. Des., **43**(15), pp. 1169–1178.

[123] Kilic, B., Agwai, A., and Madenci, E., 2009, "Peridynamic Theory for Progressive Damage Prediction in Center-Cracked Composite Laminates," Compos. Struct., **90**(2), pp. 141–151.

[124] Sorensen, B. F., and Jacobsen, T. K., 2003, "Determination of Cohesive Laws by the J Integral Approach," Eng. Fract. Mech., **70**(14), pp. 1841–1858.

[125] Slowik, V., Villmann, B., Bretschneider, N., and Villmann, T., 2006, "Computational Aspects of Inverse Analyses for Determining Softening Curves of Concrete," Comput. Methods Appl. Mech. Eng., **195**(52), pp. 7223–7236.

[126] de Oliveira e Sousa, J. L. A., and Gettu, R., 2006, "Determining the Tensile Stress-Crack Opening Curve of Concrete by Inverse Analysis," ASCE J. Eng. Mech., **132**(2), pp. 141–148.

[127] Kwon, S. H., Zhao, Z., and Shah, S. P., 2008, "Effect of Specimen Size on Fracture Energy and Softening Curve of Concrete: Part II. Inverse Analysis and Softening Curve," Cem. Concr. Res., **38**(8–9), pp. 1061–1069.

[128] Abanto-Bueno, J., and Lambros, J., 2005, "Experimental Determination of Cohesive Failure Properties of a Photodegradable Copolymer," Exp. Mech., **45**(2), pp. 144–152.

[129] Tan, H., Liu, C., Huang, Y., and Geubelle, P. H., 2005, "The Cohesive Law for the Particle/Matrix Interfaces in High Explosives," J. Mech. Phys. Solids, **53**(8), pp. 1892–1917.

[130] Shen, B., and Paulino, G. H., 2011, "Direct Extraction of Cohesive Fracture Properties From Digital Image Correlation: A Hybrid Inverse Technique," Exp. Mech., **51**(2), pp. 143–163.

[131] Kulkarni, M. G., Geubelle, P. H., and Matou, K., 2009, "Multi-Scale Modeling of Heterogeneous Adhesives: Effect of Particle Decohesion," Mech. Mater., **41**(5), pp. 573–583.

[132] Scheider, I., 2009, "Derivation of Separation Laws for Cohesive Models in the Course of Ductile Fracture," Eng. Fract. Mech., **76**(10), pp. 1450–1459.

[133] Kulkarni, M. G., Matous, K., and Geubelle, P. H., 2010, "Coupled Multi-Scale Cohesive Modeling of Failure in Heterogeneous Adhesives," Int. J. Numer. Methods Eng., **84**(8), pp. 916–946.

[134] Zeng, X., and Li, S., 2010, "A Multiscale Cohesive Zone Model and Simulations of Fractures," Comput. Methods Appl. Mech., **199**(9–12), pp. 547–556.

[135] Tvergaard, V., 1990, "Effect of Fibre Debonding in a Whisker-Reinforced Metal," Mater. Sci. Eng., **A125**(2), pp. 203–213.

[136] Tvergaard, V., and Hutchinson, J. W., 1993, "The Influence of Plasticity on Mixed Mode Interface Toughness," J. Mech. Phys. Solids, **41**(6), pp. 1119–1135.

[137] Scheider, I., and Brocks, W., 2003, "Simulation of Cup-Cone Fracture Using the Cohesive Model," Eng. Fract. Mech., **70**(14), pp. 1943–1961.

[138] Geubelle, P. H., and Baylor, J. S., 1998, "Impact-Induced Delamination of Composites: A 2D Simulation," Compos. Part B: Eng., **29**(5), pp. 589–602.

[139] Espinosa, H. D., and Zavattieri, P. D., 2003, "A Grain Level Model for the Study of Failure Initiation and Evolution in Polycrystalline Brittle Materials. Part I: Theory and Numerical Implementation," Mech. Mater., **35**(3–6), pp. 333–364.

[140] Tvergaard, V., and Hutchinson, J. W., 1992, "The Relation Between Crack Growth Resistance and Fracture Process Parameters in Elastic-Plastic Solids," J. Mech. Phys. Solids, **40**(6), pp. 1377–1397.

[141] Wei, Y., and Hutchinson, J. W., 1997, "Steady-State Crack Growth and Work of Fracture for Solids Characterized by Strain Gradient Plasticity," J. Mech. Phys. Solids, **45**(8), pp. 1253–1273.

[142] Tvergaard, V., and Hutchinson, J. W., 2008, "Mode III Effects on Interface Delamination," J. Mech. Phys. Solids, **56**(1), pp. 215–229.

[143] Rose, J. H., Ferrante, J., and Smith, J. R., 1981, "Universal Binding Energy Curves for Metals and Bimetallic Interfaces," Phys. Rev. Lett., **47**(9), pp. 675–678.

[144] Song, S. H., Paulino, G. H., and Buttlar, W. G., 2006, "Simulation of Crack Propagation in Asphalt Concrete Using an Intrinsic Cohesive Zone Model," ASCE J. Eng. Mech., **132**(11), pp. 1215–1223.

[145] Song, S. H., Paulino, G. H., and Buttlar, W. G., 2006, "A Bilinear Cohesive Zone Model Tailored for Fracture of Asphalt Concrete Considering Viscoelastic Bulk Material," Eng. Fract. Mech., **73**(18), pp. 2829–2848.

[146] Aragao, F. T. S., Kim, Y.-R., Lee, J., and Allen, D. H., 2011, "Micromechanical Model for Heterogeneous Asphalt Concrete Mixtures Subjected to Fracture Failure," ASCE J. Mater. Civil Eng., **23**(1), pp. 30–38.

[147] Foulk, J. W., Allen, D. H., and Helms, K. L. E., 2000, "Formulation of a Three-Dimensional Cohesive Zone Model for Application to a Finite Element Algorithm," Comput. Methods Appl. Mech. Eng., **183**(1), pp. 51–66.

[148] Nutt, S. R., and Needleman, A., 1987, "Void Nucleation at Fiber Ends in Al-SiC Composites," Scr. Metal., **21**(5), pp. 705–710.

[149] McHugh, P. E., Varias, A. G., Asaro, R. J., and Shih, C. F., 1989, "Computational Modeling of Microstructures," FGCS, Future Gener. Comput. Syst., **5**(2–3), pp. 295–318.

[150] Shabrov, M. N., and Needleman, A., 2002, "An Analysis of Inclusion Morphology Effects on Void Nucleation," Model. Simul. Mater. Sci. Eng., **10**(2), pp. 163–183.

[151] Rice, J. R., and Wang, J. S., 1989, "Embrittlement of Interfaces by Solute Segregation," Mater. Sci. Eng., **A107**(1–2), pp. 23–40.

[152] Rice, J. R., 1992, "Dislocation Nucleation From a Crack Tip: An Analysis Based on the Peierls Concept," J. Mech. Phys. Solids, **40**(2), pp. 239–271.

[153] Beltz, G. E., and Rice, J. R., 1992, "Dislocation Nucleation at Metal-Ceramic Interfaces," Acta Metall. Mater., **40**(Suppl. 1), pp. S321–S331.

[154] Peierls, R., 1940, "The Size of a Dislocation," Proc. Phys. Soc., **52**(1), pp. 34–37.

[155] Sun, Y., Beltz, G. E., and Rice, J. R., 1993, "Estimates From Atomic Models of Tension-Shear Coupling in Dislocation Nucleation From a Crack Tip," Mater. Sci. Eng., **A170**(1–2), pp. 67–85.

[156] Falk, M. L., Needleman, A., and Rice, J. R., 2001, "A Critical Evaluation of Cohesive Zone Models of Dynamic Fracture," J. Phys. IV France, **11**, pp. 43–50.

[157] Finot, M., Shen, Y. L., Needleman, A., and Suresh, S., 1994, "Micromechanical Modeling of Reinforcement Fracture in Particle-Reinforced Metal-Matrix Composites," Metall. Mater. Trans., A, **25A**(11), pp. 2403–2420.

[158] Needleman, A., 1997, "Numerical Modeling of Crack Growth Under Dynamic Loading Conditions," Comput. Mech., **19**(6), pp. 463–469.

[159] Needleman, A., and Rosakis, A. J., 1999, "Effect of Bond Strength and Loading Rate on the Conditions Governing the Attainment of Intersonic Crack Growth Along Interfaces," J. Mech. Phys. Solids, **47**(12), pp. 2411–2449.

[160] Zhai, J., and Zhou, M., 2000, "Finite Element Analysis of Micromechanical Failure Modes in a Heterogeneous Ceramic Material System," Int. J. Fract., **101**(1), pp. 161–180.

[161] van den Bosch, M. J., Schreurs, P. J. G., and Geers, M. G. D., 2006, "An Improved Description of the Exponential Xu and Needleman Cohesive Zone Law for Mixed-Mode Decohesion," Eng. Fract. Mech., **73**(9), pp. 1220–1234.

[162] Klein, P. A., Foulk, J. W., Chen, E. P., Wimmer, S. A., and Gao, H. J., 2001, "Physics-Based Modeling of Brittle Fracture: Cohesive Formulations and the Application of Meshfree Methods," Theor. Appl. Fract. Mech., **37**(1–3), pp. 99–166.

[163] Volokh, K. Y., 2004, "Comparison Between Cohesive Zone Models," Commun. Numer. Methods Eng., **20**(11), pp. 845–856.

[164] Alfano, G., 2006, "On the Influence of the Shape of the Interface Law on the Application of Cohesive-Zone Models," Compos. Sci. Technol., **66**(6), pp. 723–730.

[165] Song, S. H., Paulino, G. H., and Buttlar, W. G., 2006, "Influence of the Cohesive Zone Model Shape Parameter on Asphalt Concrete Fracture Behavior," *Multiscale and Functionally Graded Material 2006 (M&FGM 2006)*, G. H. Paulino, M.-J. Pindera, R. H. Dodds, Jr., F. A. Rochinha, E. Dave, and L. Chen, eds., AIP Conference Proceedings, Maryland, pp. 730–735.

[166] Park, K., Paulino, G. H., Celes, W., and Espinha, R., 2012, "Adaptive Mesh Refinement and Coarsening for Cohesive Zone Modeling of Dynamic Fracture," Int. J. Numer. Methods Eng., **92**(1), pp. 1–35.

[167] Park, K., and Paulino, G. H., 2012, "Computational Implementation of the PPR Potential-Based Cohesive Model in ABAQUS: Educational Perspective," Eng. Fract. Mech., **93**, pp. 239–262.

[168] Park, K., 2009, "Potential-Based Fracture Mechanics Using Cohesive Zone and Virtual Internal Bond Modeling," Ph.D. thesis, University of Illinois at Urbana-Champaign, Urbana, IL.